공학박사 학위논문

Porous electrode structure for polymer electrolyte membrane water electrolysis

고분자 전해질 막 수전해용 다공성 전극 구조

2023 년 02 월

서울대학교 대학원

공과대학 화학생물공학부

강선영

Porous electrode structure for polymer electrolyte membrane water electrolysis

지도 교수 성 영 은

이 논문을 공학박사 학위논문으로 제출함
2023 년 02 월

서울대학교 대학원
공과대학 화학생물공학부
강 선 영

강선영의 공학박사 학위논문을 인준함
2023 년 02 월

위 원 장 _____ (인)

부위원장 _____ (인)

위 원 _____ (인)

위 원 _____ (인)

위 원 _____ (인)

Abstract

Porous electrode structure for polymer electrolyte membrane water electrolysis

Sun Young Kang
School of Chemical and Biological Engineering
The Graduate School
Seoul National University

Hydrogen energy has been considered as a new renewable energy source that can replace fossil fuels, because It exhibits high energy density without the emission of carbon dioxide (CO_2). Hydrogen could be mainly obtained via steam reforming, biomass conversion, and water electrolysis. Among those methods, water electrolysis has been attracting attention for sustainable hydrogen production owing to its high energy density and carbon-free emission. In this regard, the activity of electrocatalysts has been extensively studied and made significant progress. However, their excellent activity in half-cell does not guarantee the performance in single-cell, because real-world water electrolysis requires the consideration of several additional experimental factors.

While alkaline water electrolysis has been commercialized, polymer electrolyte membrane water electrolysis with a polymer electrolyte membrane including proton-exchange membrane (PEM) or anion-exchange membrane (AEM) has been considered as promising water electrolysis owing to high efficiency and high purity hydrogen production derived from the zero-gap design.

Herein, to realize superior performance in single-cell, the porous electrode structure for polymer electrolyte membrane-based water electrolysis was obtained with several approaches.

In chapter 1, we elucidate the general concept of water electrolysis using either proton exchange membrane or anion exchange membrane to clearly understand the following chapters.

In chapter 2, high-performance and stable AEMWE employing an AEM without aryl-ether backbone structure was developed. To achieve high-performance and durable AEMWE, the effect of various parameters that is suitable for the adapted AEM was investigated. As a result, the AEM adapted in this work performed much better and was more durable than the conventional AEM (FAA-3). Moreover, it exhibited high efficiency under pure water feeding conditions. These results were attributed to high-efficient and durable AEM caused by its absence of aryl-ether backbone. This work suggests the potential use of polyphenylene structure as aryl-ether free backbone of AEM on AEMWE operated using alkaline solution and/or pure water.

In chapter 3, a three-dimensional porous NiFe/Ni foam electrode was developed for AEMWEs. The electrodes were directly fabricated by a one-step electro-deposition (ED) process with direct-current and pulse-current applying processes. This ionomer-free electrode, without the use of non-electronic conductive polymer material, showed higher performance owing to the lower ohmic resistance than the conventional particle-based electrode. The three-dimensional porous structure effectively enhanced the specific surface area and decreased mass transport resistance. With those beneficial composition and structure, the AEMWE revealed superior performance, which showed 3.87 A cm^{-2} at 1.9 V, and a small increased overpotential (11.1 mV h^{-1}), compared to the conventional or non-porous electrode.

In chapter 4, an iridium nickel oxide directly coated anode ($IrNiO_x$ electrode) for high-efficient PEMWE was developed. Five $IrNiO_x$ electrodes with different ratio

of Ir to Ni were developed using co-electrodeposition. The resulting electrodes consist of thin $IrNiO_x$ layer on the carbon substrate. To develop the PEMWE incorporating $IrNiO_x$ electrode, the effect of fabrication methods, catalyst compositions, and porous transport layer (PTL) were investigated. As a result, the $IrNiO_x$ prepared with 7: 3 precursor solution ($Ir_{0.5}Ni_{0.5}O_x$) exhibited higher OER activity with smaller overpotential compared to that prepared with 10: 0 precursor solution (IrO_x) and the commercial IrO_2. Also, the performance of PEMWE with the $Ir_{0.5}Ni_{0.5}O_x$ electrode was higher than that with the sprayed electrode using commercial IrO_2 nanoparticles. This enhancement is attributed to the increased electrochemical surface area due to the introduction of Ni in the Ir. Additionally, the performance of the directly coated $Ir_{0.5}Ni_{0.5}O_x$ PEMWE is the highest performance reported in the literature.

Keywords: proton exchange membrane water electrolyzer, anion exchange membrane water electrolyzer, porous structure, durability of water electrolysis

Student Number: 2019-30419

Table of Contents

List of Figures

Chapter 1. Introduction

1.1. General introduction of water electrolysis

Hydrogen can be produced renewably using a variety of methods such as steam reforming [1.2], photoproduction [3], and water electrolysis [4,5]. Among those methods, water electrolysis has attracted much attention owing to its high efficiency and high-purity hydrogen production [4,5]. In water electrolysis system, water is split into oxygen (anode) and hydrogen (cathode) gases with the following chemical reaction. Depending on the types of electrolyte, i.e. alkaline and acidic, the water electrolysis is operated through different mechanism.

<In alkaline>

Anode $2OH^- \rightarrow H_2O + 2e^- + 1/2O_2$ $E^0 = 1.229$ V

Cathode $2H_2O + 2e^- \rightarrow 2OH^- + H_2$ $E^0 = 0.000$ V

Overall $H_2O \rightarrow 1/2O_2 + H_2$ $E^0 = 1.299$ V

<In acid>

Anode $H_2O \rightarrow 2H^+ + 1/2O_2 + 2e^-$ $E^0 = 1.229$ V

Cathode $2H^+ + 2e^- \rightarrow H_2$ $E^0 = 0.000$ V

Overall $H_2O \rightarrow 1/2O_2 + H_2$ $E^0 = 1.229$ V

Water electrolysis could be classified by the types of electrolyte: alkaline electrolysis (AWE) and polymer electrolyte membrane water electrolysis such as proton exchange membrane water electrolysis (PEMWE) and anion exchange membrane water electrolysis (AEMWE). AWE, operated with liquid alkaline solution as electrolyte, has been commercialized. Employing non-noble materials i.e. Ni, Co, Fe as electrode could reduce the cost. However, AWE has some disadvantages such as low efficiency, low stability, low purity of hydrogen, and

electrolyte leakage problems [6,7]. To overcome the drawbacks of AWE, PEMWE was developed. PEMWE has the highest efficiency and stability because the PEM exhibits high ionic conductivity and stability. Additionally, the high purity of hydrogen could be obtained owing to the absence of liquid at the cathode where the hydrogen gas is produced. Despite these advantages, the high cost of PEMWE is considered an obstacle to its commercialization. Highly active oxygen evolution reaction (OER) catalysts have been widely proposed to improve the performance of the PEMWE, and Ir is well-known for effective OER catalyst in an acid electrolyte. Therefore, introducing transition metals on Ir as a type of alloy has been investigated to increase the OER activity and decrease Ir loading [8,9]. AEMWE, water electrolysis with an anion-exchange membrane (AEM), has been developed as an alternative to improve the drawbacks of AWE and PEMWE in recent years [10,11]. The schematic diagram of AEMWE was indicated in Figure 1.1.1. AEMWE combines advantages of AWE and PEMWE. It shows higher efficiency and purity of produced hydrogen than AWE owing to the use of an AEM rather than a liquid electrolyte. In addition, its cost is potentially lower than that of PEMWE as non-noble metal-based materials can be applied. Nevertheless, it is reported that its performance and durability are still low compared to those of PEMWE, as the recently developed AEM exhibits low ionic conductivity and stability. Moreover, only few studies investigating the membrane-electrode assembly have been reported.

Figure 1.1.2 indicates the comparison in performance of three water electrolysis [12]. AWE exhibits the lowest performance due to the use of alkaline solution as electrolyte, causing large ohmic resistance. In contrast, PEMWE shows the highest efficiency owing to the well-verified high performance and durable membrane, Nafion. Although its high performance, high cost of platinum group noble materials on electrodes such as Pt, Ir and Ru has been developed. The performance of AEMWE is between that of AWE and PEMWE. Although AEMWE also adopt the membrane, the AEM and anion-exchange ionomers still shows poor anion

conductivity and stability. Therefore, the AEMWE exhibits lower performance than PEMWE. Further development of AEM can be expected to enhance performance of AEMWE.

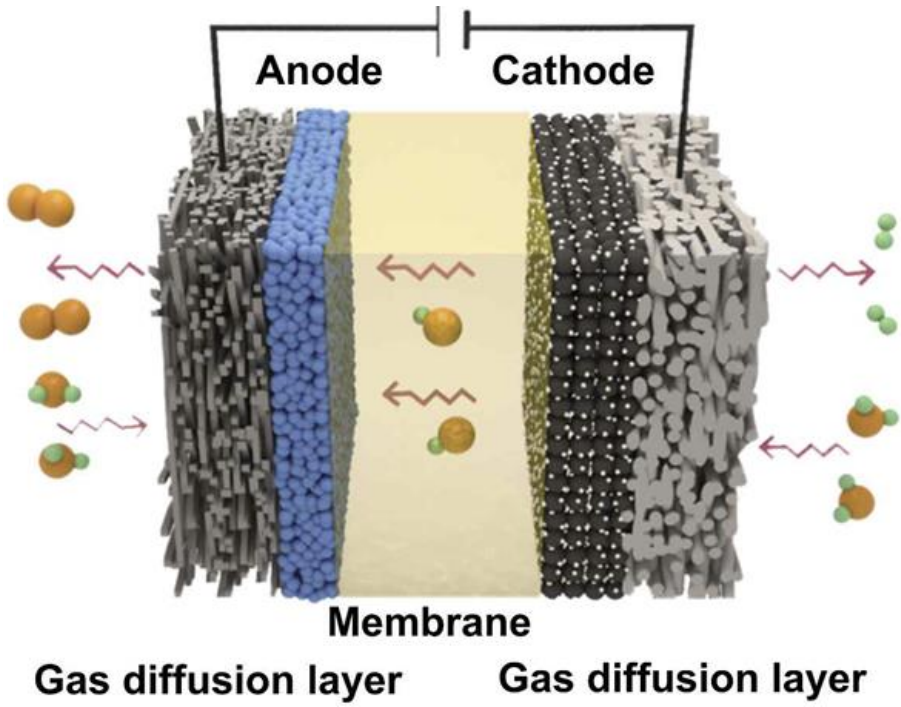

Figure 1.1.1 Schematic diagram of anion exchange membrane water electrolysis

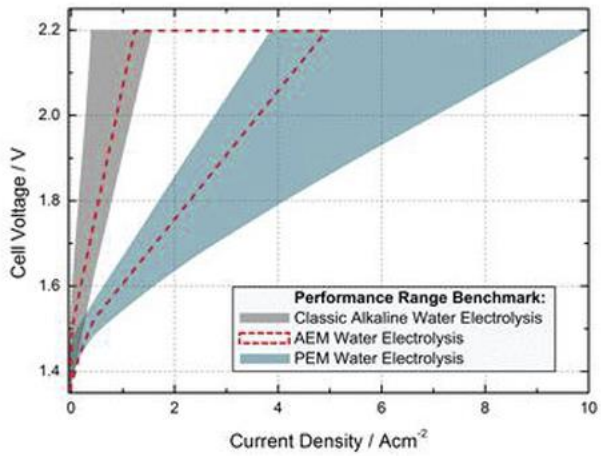

Figure 1.1.2 The comparison in performance of three water electrolysis (AWE, PEMWE, and AEMWE). Reprinted with permission from ref 12

1.2. Aim of this thesis

Even though hydrogen with high purity and sustainable could be produced by water electrolysis, the commercialization of water electrolysis is hindered due to the low performance and high cost. To overcome these drawbacks, highly efficient water electrolysis should be developed. To achieve highly efficient and low-cost polymer electrolyte membrane water electrolysis, enhance electrochemical kinetics with maximize utilization of catalyst and mass transfer with facilitating the flow of reactants and products. The porous structure can be the one that satisfies both by improving specific surface area of catalyst and offering pathway to transfer reactants and products.

The aim of this thesis is to investigate the effect of porous structure by using following strategies: (1) controlling contents of ionomer (2) porous structure from the fabrication of process (3) porous electrode using metal leaching. These fabrication processes are facile with simple equipment. To achieve high performance anion-exchange membrane water electrolysis, optimized ionomer contents and water electrolyzer component and operation parameters were investigated. In addition, the enhanced electronic conductivity catalyst utilization was achieved from ionomer-free composition and porous electrode. The micropores was also developed using the operating condition of PEMWE without additional process of leaching removable metal.

1.3. References

[1] S. Dutta, A review on production, storage of hydrogen and its utilization as an energy resource, Journal of Industrial and Engineering Chemistry, 20 (2014) 1148-1156.

[2] J.A. Turner, A realizable renewable energy future, Science, 285 (1999) 687-689.

[3] J.A. Turner, Sustainable hydrogen production, Science, 305 (2004) 972-974.

[4] Y. Wang, K.S. Chen, J. Mishler, S.C. Cho, X.C. Adroher, A review of polymer electrolyte membrane fuel cells: Technology, applications, and needs on fundamental research, Applied energy, 88 (2011) 981-1007.

[5] H. Zhang, P.K. Shen, Recent development of polymer electrolyte membranes for fuel cells, Chemical reviews, 112 (2012) 2780-2832.

[6] M. Carmo, D.L. Fritz, J. Mergel, D. Stolten, A comprehensive review on PEM water electrolysis, International journal of hydrogen energy, 38 (2013) 4901-4934.

[7] S.S. Kumar, V. Himabindu, Hydrogen production by PEM water electrolysis–A review, Materials Science for Energy Technologies, 2 (2019) 442-454.

[8] Z. Chen, X. Duan, W. Wei, S. Wang, B.-J. Ni, Electrocatalysts for acidic oxygen evolution reaction: Achievements and perspectives, Nano Energy, 78 (2020) 105392.

[9] H. Wu, Y. Wang, Z. Shi, X. Wang, J. Yang, M. Xiao, J. Ge, W. Xing, C. Liu, Recent developments of Iridium-based catalysts for oxygen evolution reaction in acidic water electrolysis, Journal of Materials Chemistry A, (2022).

[10] T. Mennola, M. Mikkola, M. Noponen, T. Hottinen, P. Lund, Measurement of ohmic voltage losses in individual cells of a PEMFC stack, Journal of power sources, 112 (2002) 261-272.

[11] J.M. Sierra, S.J. Pathiyamattom, S. Gamboa, Study of activation losses and ohmic resistance in a PEM fuel cell using computational fluid dynamics, ECS Transactions, 20 (2009) 395.

[12] M. Carmo, D.L. Fritz III, W. Maier, D. Stolten, Alkaline water electrolysis vs. PEM water electrolysis-exploring their full performance, Electrochemical Society Meeting Abstracts 227, The Electrochemical Society, Inc., 2015, pp. 1489-1489.

Chapter 2. High-performance and durable water electrolysis using highly conductive and stable anion-exchange membrane

2.1. Introduction

As the global warming problem arises, hydrogen energy has been considered as a new renewable energy source that can replace fossil fuels. It exhibits high energy density without the emission of carbon dioxide (CO_2). Consequently, water electrolysis has attracted attention as a hydrogen-production process owing to being a high-efficiency and environmentally friendly method [1,2]. Moreover, it can be linked with the renewable energies such as solar and wind power, for power generation. Various reports have been published on this study, and two types of water electrolysis have been mainly developed: alkaline water electrolysis (AWE) and proton-exchange membrane water electrolysis (PEMWE) [3]. AWE operates using liquid electrolytes and has been commercialized owing to its low cost and simplicity. However, AWE has drawbacks such as low efficiency, low stability, low purity of hydrogen, and leakage problems. In addition, PEMWE, which employs a proton-exchange membrane (PEM), exhibits high efficiency and high-purity hydrogen production. As PEMWE operates in an acidic atmosphere, the use of noble metals such as iridium (Ir), ruthenium (Ru), and titanium (Ti) as catalysts, a liquid/gas diffusion layer (LGDL), and bipolar plates were required, leading to an increase in costs [3,4].

Anion-exchange membrane water electrolyte (AEMWE) has been recently developed as an alternative to conventional water electrolysis [5,6]. AEMWE integrates AWE with PEMWE to improve the disadvantages of the two previously mentioned electrolysis methods [6]. In AEMWE, water is reduced to produce hydrogen and hydroxide ions at the cathode. Then, hydroxide ions diffuse through

the AEM and oxidize to produce water and oxygen at the anode by losing electrons as given by the following equations.

Anode: $4OH^- \rightarrow O_2 + 2H_2O + 4e^-$, $E_0 = -0.828\ V_{SHE}$ (1)

Cathode: $4H_2O + 4e^- \rightarrow 2H_2 + 4OH^-$, $E_0 = 0.401\ V_{SHE}$ (2)

Overall: $2H_2O \rightarrow 2H_2 + O_2$, $E_0 = 1.229\ V_{SHE}$ (3)

It shows higher efficiency and purity of produced hydrogen than AWE owing to the use of an anion-exchange membrane (AEM) rather than a liquid electrolyte. In addition, its cost is potentially lower than that of PEMWE as non-noble metal-based materials can be applied. Nevertheless, it is reported that its performance and durability are still low compared to those of PEMWE, as the recently developed AEM exhibits low ionic conductivity and stability [7,8]. Thus, it is important to investigate various commercial AEMs exhibiting high AEMWE performance and durability. In addition to the development of a highly conductive, physically and chemically stable AEM, it is essential that the investigation of membrane-electrode assembly (MEA) components and operating conditions to obtain superb performance AEMWEs.

As public interest is rising, numerous studies have focused on the development of optimal MEA components using commercial AEMs for high-performance AEMWE. Various commercial AEMs, such as A201® (Tokuyama Co., Japan), Fumapem® (Fumatech Co., Germany), Sustainion® (Dioxide Materials Co., USA), Aemion™ (Ionomr Innovation Co., Canada), and Orion TM1™ (Orion Polymer, USA), have been recently developed and commercialized. For A201®, which was an early developed product and has been discontinued, AEMWE showed a low performance of 350–550 mA cm^{-2} at 1.9 V_{cell} [9-11]. Park et al. [12] applied a Fumapem® membrane in AEMWE and investigated the effect of fabrication methods, operating conditions, and MEA parameters; they achieved AEMWE with a performance of 1500 mA cm^{-2} at 1.9 V_{cell}. However, it is well known that the use of A201® and Fumapem® as AEMs leads to the low durability of AEMWE.

Dioxide Materials Co. developed the Sustainion® membrane and reported its performance and durability in AEMWE [13]; they enhanced the AEMWE performance by two times compared to that using FAS–50® (Fumatech Co., Germany). While FAS–50® showed a sharp voltage increase for 180 h, it showed durable performance for 1950 h. Fortin et al. [14] proposed AEMWE with the Aemion™ membrane, exhibiting a performance of 2000 mA cm^{-2} at 1.82 V at 60 °C. They also achieved high durability with a degradation rate of 3.21 mV h^{-1} at 50 °C. AEMWEs using most AEMs except Orion TM1™ have been examined.

Here, we report high-performance and durable AEMWE using the commercial Orion TM1™ membrane. This is the first report applying Orion TM1™ membrane on AEMWE. The Orion TM1™ membrane contains quaternary ammonium as a functional group and a polyphenylene as backbone, and it is reported to show high ionic conductivity and stability [15]. The hydrophobicity and geometry of the membrane facilitate to form microstructure, which effectively improved performance of AEMWE by enhanced ion transportation. The aryl-ether free backbone feature is also supposed to show improved stability preventing decomposed by OH^- attack. In addition to the development of the AEM, it is important to investigate the MEA parameters that greatly influence the AEMWE performance. Ionomer contents, catalyst loadings, temperatures, and types of feeding solutions have been investigated to achieve the MEA parameters that are suitable for the Orion TM1™ membrane. Further, the performance and durability of AEMWE using the Orion TM1™ membrane have been evaluated by comparing it with conventional AEMs with different temperature and stability test protocols i.e. constant current and potential cycling mode. To exclude the effect of the catalytic activity, high-active and stable noble metal-based catalysts were employed for anode and cathode.

2.2. Experimental

Physicochemical characterizations

Thermogravimetric analysis (TGA; TA Instruments, SDT Q600, USA) was performed under N_2 in a temperature range of 50 to 900 °C at the heating rate of 10 °C min^{-1} to examine thermal stability of the membranes. Fourier-transform infrared (FT-IR) spectroscopy was performed on a spectrometer (TENSOR27, Bruker, Germany), which is installed at the National Center for Inter-University Research Facilities (NCIRF) at Seoul National University, in a transmittance mode. The conductivity of AEMs were measured by EIS analysis. 0.2 mg_{Pt} cm^{-2} of 40 wt.% of Pt/C catalyst were applied to both FAA-3 and Orion TM1™ membranes by spraying method. Fully humidified H_2 and N_2 gas were provided to the anode and cathode respectively at a rate of 200 ml min^{-1}. The EIS measurement for ionic resistance, was conducted at 0.45 V_{cell}, which is non-faradaic condition, for a frequency range of 50 mHz to 100 kHz with an amplitude of 5 mV.

Preparation of the MEA

The schematic diagram of a single-cell is illustrated in Fig. 2.2.1. Prior to use of two AEMs, those were immersed in 1.0 M of potassium hydroxide solution (KOH, SAMCHUN Chemical, Republic of Korea) for 3 h to replace bromide with hydroxide, and thoroughly rinsed with DI water for 1 h. To fabricate the MEA, the catalyst slurry was directly coated to the membrane by spraying method, as described in our previous study [16]. To fabricate catalyst layers (CLs), the catalyst slurry containing catalyst nanoparticles, de-ionized water, isopropyl alcohol (IPA, Sigma Aldrich, USA), and FAA-3-Br solution (Fumatech Co., Germany) was sprayed on each side of the membrane. The 40 wt.% Pt/C (Johnson Matthey, UK) with 0.2, 0.4, and 0.6 mg_{Pt} cm^{-2} of metal loading amount and iridium oxide (Premion®, Alfa Aesar, USA) with a loading amount of 1.0, 2.0, 3.0 mg cm^{-2} were employed as catalyst nanoparticles for the anode and cathode, respectively. For AEM, the 50 μm of FAA-3-50® membrane (Fumatech Co., Germany) and 30 μm of

Orion TM1™ membrane were used. The active area of the electrode was 5 cm^2. For the comparison of the effect of AEMs, the same electrode composition was adopted. For the cathode, 0.4 mg_{Pt} cm^{-2} with 30 wt.% of ionomer were adopted, and 2 mg_{IrO_2} cm^{-2} with 10 wt.% of ionomer were employed for the anode.

Field emission scanning electron microscopy

The morphology of the fabricated catalyst layer was investigated by field emission scanning electron microscopy (FE-SEM; SUPRA 55VP, Carl Zeiss, Germany). In order to obtain cross-section views of the MEAs using FE-SEM, the MEAs were immersed in liquid nitrogen, and thereafter the frozen ones were broken with tweezers.

Single-cell performance test

For the single-cell performance test of AEMWE, titanium felt (CNL Energy, Republic of Korea) and carbon paper with a microporous layer (JNT40-A3, JNTG Co., Republic of Korea) were used as the anode and cathode LGDLs, respectively, without further treatment. The single-cell unit (CNL Energy, Republic of Kora) was assembled with the fabricated MEAs, LGDLs, and the titanium bipolar plates with a serpentine flow field. The temperature of the single-cell was maintained at 50, 60, 70, and 80 °C, and 1.0 M of KOH was constantly supplied to both the anode and cathode at a rate of 1.0 ml min^{-1}. These conditions were adopted for all experiments unless otherwise noted. To evaluate the single-cell performance, the linear sweep voltammetry method was adopted, and voltage in the range of 1.35 to 2.15 V_{cell} was applied at a scan rate of 5 mV s^{-1} using an electrochemical workstation (ZENNIUM, ZAHNER-Elecktrik GmbH & Co. KG, Germany). Electrochemical impedance spectroscopy (EIS) was performed to measure the internal resistances at the same electrochemical workstation but at different modes. The EIS measurements were performed at 1.9 V_{cell} for a frequency range of 100 mHz to 100 kHz with an amplitude of 5 mV. To investigate the stability of AEMWE, chronopotentiometric measurements were conducted at a constant current density of 500 mA cm^{-2} for 10

h and 50 h, and the test was cut off if the cell voltage exceeded 2.3 V_{cell} with electrolytic cell test system (CNL Energy, Republic of Korea). The cycling-based stability of AEMWE was performed by repeating for 200 cycles the linear sweep voltammetry method as conducted in the single-cell performance. The amount of produced hydrogen during stability test was also measured with the same instrument.

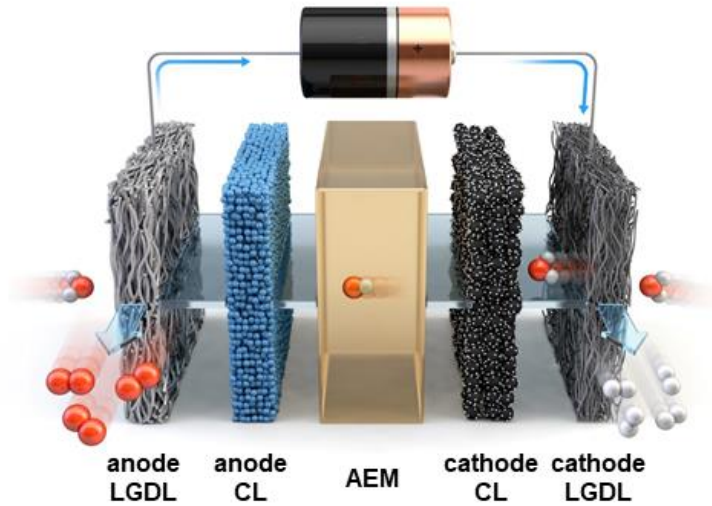

Figure 2.2.1 Schematic diagram of the membrane-electrode assembly (MEA) (liquid gas diffusion layer (LGDL) and catalyst layer (CL). H and O atoms are illustrated as red and white ball, respectively.

2.3. Results and discussion

Physicochemical characterization of Orion TM1™ and FAA-3.

Fig. 2.3.1(a) represents the chemical structure of the Orion TM1™. While the FAA-3 membrane includes the ether bond in the backbone structure [17], the Orion TM1™ membrane does not contain one. It is well known that the ether bond is subjected to the OH^- attack, leading to the degradation of AEM under operation condition [18,19]. This implies that the Orion TM1™ membrane could be more durable AEM compared to FAA-3 membrane under the AEMWE operation. In addition, thermal stabilities of the AEMs were investigated using TGA. As shown in Fig. 2.3.1(b), the both showed a slight weight loss above 100 °C, which is ascribed to the water molecules from the polymer matrix of moisture. The first weight loss step at approximately 250 °C is attributed to the unstable side chains removed from the main chain. The second step, which is more rapid step, is mainly ascribed from the decomposition of the polymer backbone structure. The temperature Orion TM1™ membrane is clearly higher than FAA-3 membrane, suggesting that higher thermal stability of the polymer structure. Fig. 2.3.1(c) shows the FT-IR spectrum of FAA-3 and Orion TM1™ membrane. The broad peak indicated in both membranes at 3200 - 3600 cm^{-1} is attributed to the O-H stretching of the water molecules absorbed into the membrane implying the hydrophilicity of them. The characteristic peaks of the asymmetric stretching of the diphenyl ether group obviously appeared at 1302 and 1185 cm^{-1} [20]. The appearance of two bands at 1476 and 795 cm^{-1} corresponds to the C-C aromatic stretching [21]. Total ohmic resistance is the sum of electrical resistances, contact resistances between cell components and ionic resistance of membrane. The electrical and contact resistances were assumed to identical because the same cell components are used with same instrument except for the membrane. The electrical resistances were measured as 3.70 mΩ. Thus, residual ohmic resistance could be considered as ionic resistance of AEM. As indicated in Fig. 2.3.2, the resistance of Orion TM1™ (1.30

mΩ cm^2), was definitely lower than that of FAA-3 (1.70 mΩ cm^2) implying higher ionic conductivity of Orion TM1™ membrane than FAA-3.

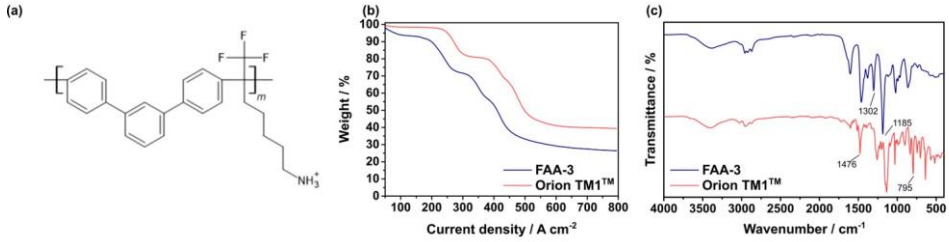

Figure 2.3.1 (a) Chemical structure of Orion TM1™ membrane. (b) TGA spectrum of FAA-3 and Orion TM1™ membrane as a function of temperature at a heating rate of 10 °C min^{-1}. (c) FT-IR spectra of FAA-3 and Orion TM1™ membrane.

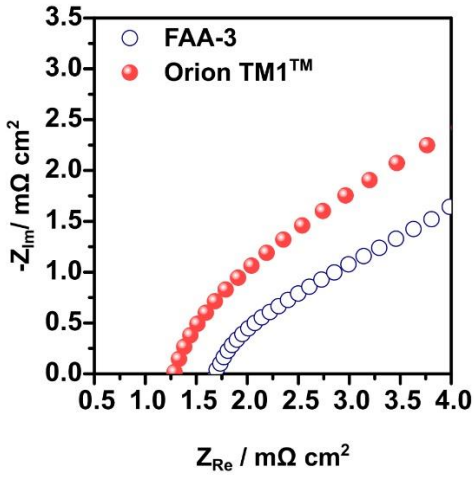

Figure 2.3.2 Nyquist plots of AEMWEs with FAA-3 and Orion TM1™ membrane. Hydrogen and nitrogen were supplied to anode and cathode respectively, under relative humidity of 100%. The temperature of the single-cell was maintained at 70 ^{o}C.

Effect of ionomer contents

The ionomer in the catalyst layer not only transports hydroxide ions between active sites and the membrane but also binds the catalyst particles forming secondary pores [22]. If the ionomer is insufficient, some hydroxide ions may not have access to the active site where the actual electrochemical reaction occurs. The utilization of a catalyst is thus inhibited, thereby reducing performance. However, too much ionomer content interrupts the electrochemical reaction because low electro-conductive ionomer inhibits electrons moving to the active sites [23]. Thus, the achievement of a proper ionomer content is essential for high-performance AEMWE. The effects of the ionomer content in the cathode and anode were investigated. First, the cathode ionomer content was examined. Most studies have focused on the effect of the anode ionomer content for PEMWE [24,25]. However, the kinetic of hydrogen evolution reaction (HER) in alkaline electrolyte is more sluggish than that in acid electrolyte. Thus, investigation of the cathode ionomer content is also crucial for AEMWE. Different cathode ionomer contents of 10, 20, 30, and 40 wt.% (hereafter, denoted by cI-10, cI-20, cI-30, and cI-40, respectively) were applied in the MEAs. The anode ionomer content of 20 wt.% was constant. Fig. 3(a) presents the polarization curves of the four AEMWEs (cI-10, cI-20, cI-30, and cI-40). As indicated in Fig. 2.3.3(a), the current densities at 1.9 V_{cell} of cI-10, cI-20, cI-30, and cI-40 were 1.72, 1.92, 2.40, and 1.38 A cm^{-2}, respectively. When the ionomer content increased from 10 to 30 wt.%, the performance gradually increased, and when the ionomer content increased further to 40 wt.%, the performance decreased. These results correspond to the EIS analysis shown in Fig. 2.3.3(b). In the Nyquist plots, the intercept with the real axis at high frequency indicates the ohmic resistance, and the size of the semicircle is mainly associated with the magnitude of the activation and mass transport resistance, derived from the catalytic reaction and mass transportation of the reactant and product [26]. The cell performance increase from cI-10 to cI-30 was owing to the low activation resistance. The increased ionomer content resulted in reduced activation resistance,

leading to an increase in cell performance. In contrast, the activation, ohmic, and mass transport resistances of cI-40 exceeded those of the other AEMWEs. This is attributed to the fact that the excessive ionomer disturbed the electrochemical reactions by blocking the electron pathway in the single cell. Therefore, cI-30 showed the highest current density and apparently the smallest resistances, including the activation, ohmic, and mass transport resistances. In this regard, the proper ionomer ratio that provides secondary pores and enlarges catalyst utilization is determined to be 30 wt.% for the cathode.

In addition, the anode ionomer content was also investigated. Unlike in the cathode, catalyst nanoparticles themselves without the use of carbon support were used as the anode catalysts owing to the carbon corrosion issue under water electrolysis operation conditions [27,28]. Fig. 2.3.3(c) shows the performances of AEMWEs with different amounts of ionomer, i.e., 5, 10, 20, 30, and 40 wt.% (hereafter, denoted by aI-05, aI-10, aI-20, aI-30, and aI-40, respectively), in the anode. The cathode ionomer content was fixed to 30 wt.%, as discussed above. The performance of AEMWEs with different anode ionomer contents increased from aI-05 to aI-10 but decreased from aI-10 to aI-40. This is because, as mentioned above, a certain amount of ionomer assists the electrochemical reaction by facilitating the hydroxide ions in the catalyst layer, but excessive ionomer blocks the active sites of the catalyst. As shown in Fig. 2.3.3(d), aI-05 shows large activation and mass transport resistance owing to the very small ionomer content. Additionally, the catalyst layer of aI-05 exhibits a dense catalyst structure with small secondary pore sizes, inhibiting transport of the reactant and product (Fig. 2.3.4(a)). In contrast, as the ionomer content increased from 5 to 10 wt.%, the cell performance improved, and activation and mass transport resistance reduced, indicating that the 10 wt.% is sufficient content for efficient ionic connection. For an ionomer content > 10 wt.%, the cell performance was reduced. This is because high ionomer content led to larger secondary pores (Fig. 2.3.4(b) and (c)), but excess ionomer covered the catalyst surface, as shown in Fig. 2.3.4(d) and (e),

leading to reduced performance of AEMWE. Thus, an ionomer content of 10 wt.% was determined to be the optimal content for achieving high performance and low resistances.

As a result of the investigation, the optimal ionomer contents of the cathode and anode were 30 and 10 wt.%, respectively. The 40 wt.% Pt/C employed as the cathode catalyst in this study consists of several nanometers of platinum particles supported on the tens of nanometers of the sphere-shaped carbon surface [29]. Most of the ionomers cover the carbon surface, and there is little amount of ionomer presence on the platinum particles [30,31], which may require more ionomer than unsupported catalyst nanoparticles. On the other hand, the ionomer in the IrO_2 anode catalyst layer, which is irregularly shaped and/or sized [29], is prone to directly covering the surface of the catalyst nanoparticle, blocking the active sites of IrO_2. Thus, the optimal ionomer content for the anode was found to be lower than that for the cathode.

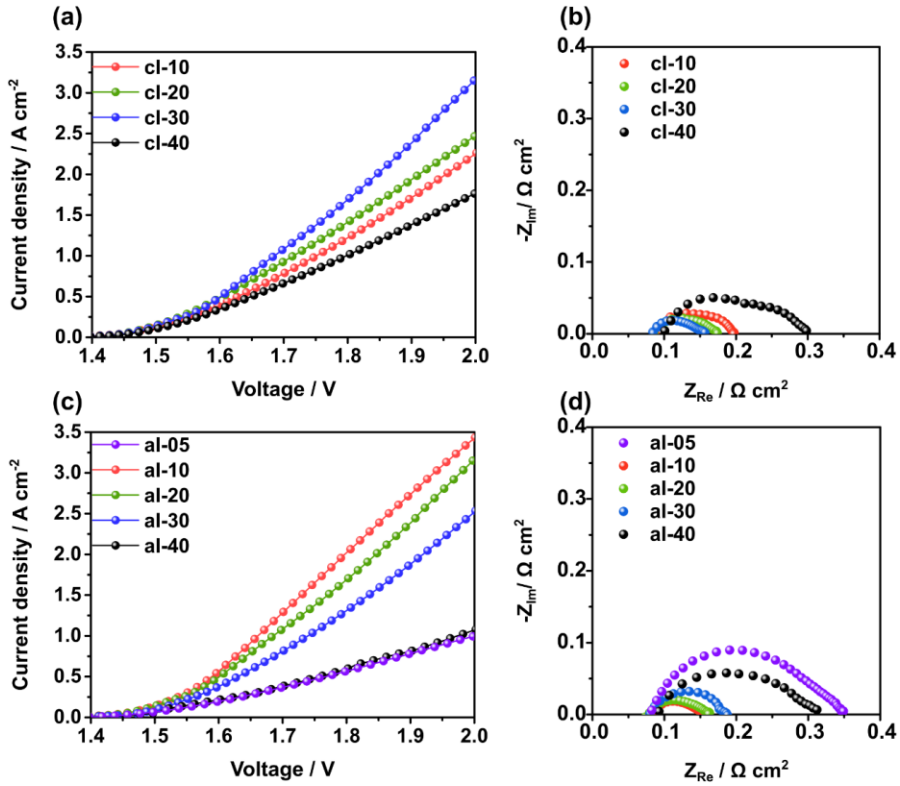

Figure 2.3.3 (a) Polarization curves and (b) Nyquist plots obtained at 1.9 V_{cell} of AEMWEs (cI-10, -20, -30, and -40) with different cathode ionomer contents of 10, 20, 30, and 40 wt.%. The anode ionomer content was constant at 20 wt.%. (c) Polarization curves and (d) Nyquist plots obtained at 1.9 V_{cell} of AEMWEs (aI-05, -10, -20, -30, and -40) with different anode ionomer contents of 5, 10, 20, 30, and 40 wt.%. The cathode ionomer content was constant at 30 wt.%.

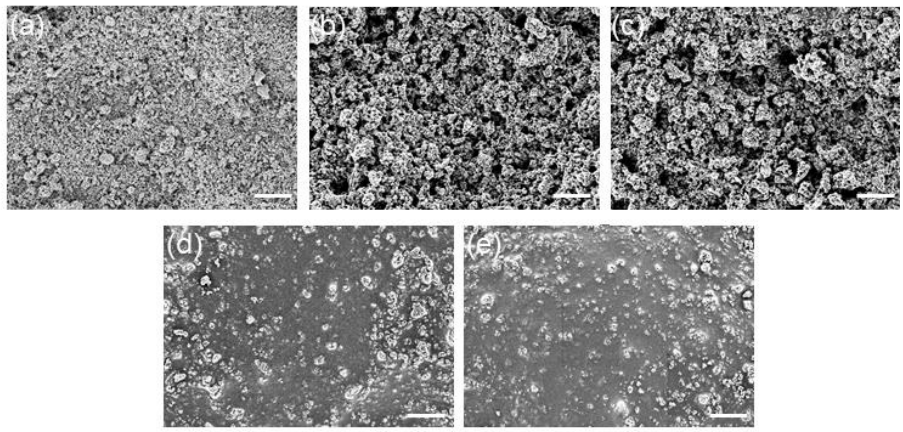

Figure 2.3.4 FE-SEM images of anode catalyst layer surface fabricated with (a) 5 (b) 10 (c) 20 (d) 30 and (e) 40 wt.% of ionomer contents. The scale bar represents 2 μm.

Catalyst loadings

To examine the effect of the cathode catalyst loading, three different loadings of Pt/C catalyst, which show high activity for HER, were applied to the cathodes (0.2, 0.4, and 0.6 mg_{Pt} cm^{-2}; hereafter, denoted by cL-0.2, cL-0.4, and cL-0.6, respectively). Fig. 2.3.5 shows the polarization curves and Nyquist plots with different catalyst-loaded MEAs. As shown in Fig. 2.3.5(a), cL-0.2 showed the lowest performance in the overall voltage range. From the Nyquist plot of cL-0.2, a second semicircle can be observed, which results from the slow reaction kinetics of the HER. cL-0.6 shows the highest performance in the low-voltage region (0.38 A cm^{-2} at 1.55 V_{cell}) compared with cL-0.2 and cL-0.4 (0.29 and 0.30 A cm^{-2}), for which the catalytic kinetics dominantly affected by the loading of the catalyst [32]. In the middle- and high-voltage regions, however, cL-0.6 exhibits lower current density (2.19 A cm^{-2} at 1.9 V_{cell}) than cL-0.4 (2.75 A cm^{-2}). This is due to the thicker catalyst layer of cL-0.6 because of the high catalyst loading. A loading of 0.4 mg_{Pt} cm^{-2} exhibited the highest performance because of the lowest resistance of the cathode.

The effect of the anode catalyst loadings was likewise examined evaluating the performance of MEAs with three IrO_2 loadings of 1, 2, and 3 mg_{IrO2} cm^{-2} (hereafter, denoted by aL-1, aL-2, and aL-3, respectively) (Fig. 2.3.5(c)). It can be expected that the aL-3 shows the highest performance owing to the high loading of the IrO_2 catalyst. Nevertheless, the current density of aL-3 is lower than those of aL-1 and aL-2 when the voltage exceeds 1.87 V_{cell}. As shown in Nyquist plots (Fig. 2.3.5(d)), the size of the semicircle of aL-3 is the largest, implying the greatest resistance. This is attributed to the large mass transport resistance derived from the thick anode catalyst layer. As indicated in Fig. 2.3.6(a)-(c), the thickness of aL-1, aL-2, and aL-3 were 4.79, 10.11, and 12.52 μm, respectively. The excessive catalyst not only significantly increases the price of AEMWE but also makes the catalyst layer thicker, preventing the transportation of the reactant and product. Considering the

industrial application of AEMWE under high current densities, cL-0.4 and aL-2 may be more advantageous than cL-0.6 and aL-3. Especially for anode catalyst loading of water electrolysis, 2.0 to 3.8 mg cm^{-2} of high loading are often demanded owing to the more sluggish OER compared with HER [14,33,34]. Therefore, the use of the optimal amount of catalyst improves the performance and has a significant impact on reducing the cost of AEMWE. In our study, the optimum catalyst loading was found to be 0.4 mg_{Pt} cm^{-2} and 2.0 mg_{IrO_2} cm^{-2} for the cathode and the anode, respectively.

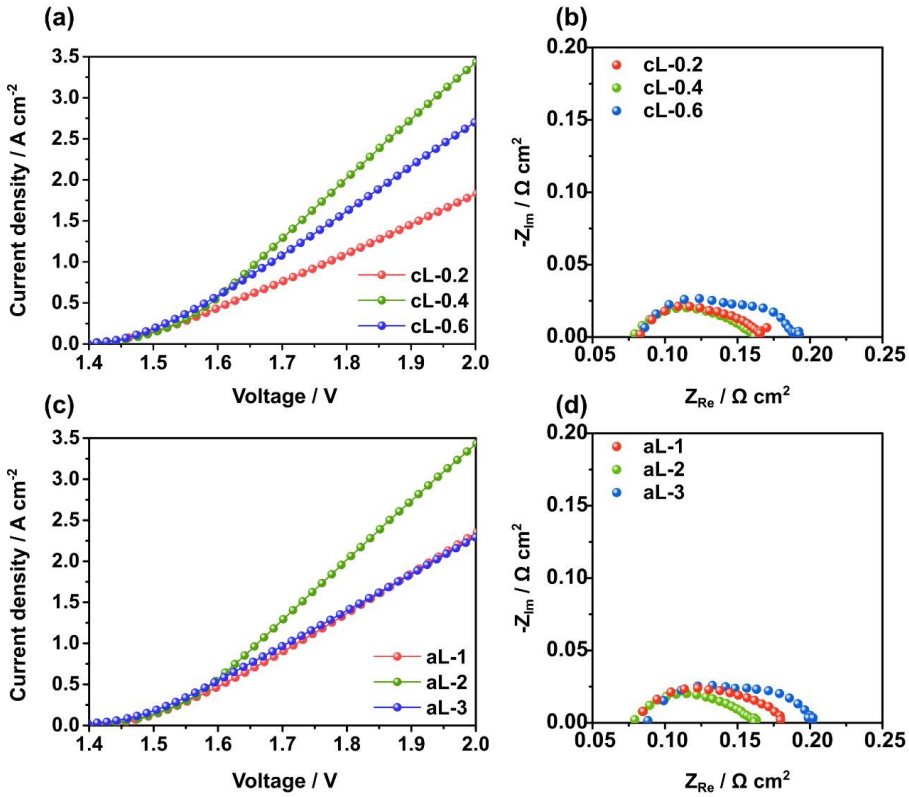

Figure 2.3.5 (a) Polarization curves and (b) Nyquist plots obtained at 1.9 V_{cell} of AEMWEs (cL-0.2, -0.4, and -0.6) with different cathode catalyst loadings of 0.2, 0.4, and 0.6 mg_{Pt} cm^{-2}. The anode loading was constant at 2 mg_{IrO2} cm^{-2}. (c) Polarization curves and (d) Nyquist plots obtained at 1.9 V_{cell} of AEMWEs (aL-1, -2, and -3) with different anode catalyst loadings of 1, 2, and 3 mg_{IrO2} cm^{-2}. The cathode loading was constant at 0.4 mg_{Pt} cm^{-2}.

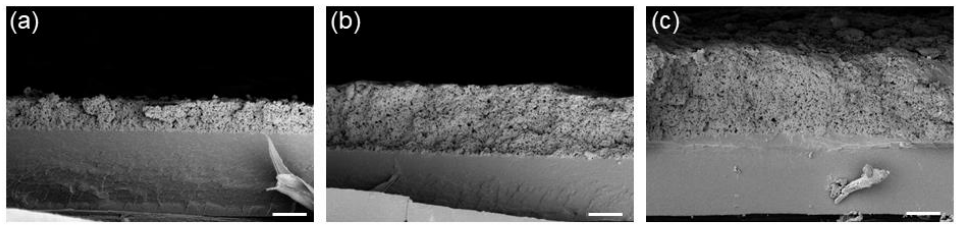

Figure 2.3.6 FE-SEM images of anode catalyst layer cross-section with (a) 1 (b) 2 and (c) 3 mg cm^{-2} of loadings. The scale bar represents 5 μm.

Effect of cell temperatures

Using the optimized MEA parameters, investigation of two AEMWEs with the Orion TM1™ membrane and FAA-3 membrane, which exhibits high performance according to our previous study [12], operating under different conditions is crucial for examining the effect of the AEM on AEMWE. First, we examined the effect of the cell temperature on the AEMWE performance. The operating temperature needs to be less than 100 °C because the water-based solution is fed to AEMWE, and the AEM could degrade within this range. For example, Chen et al. [35] reported that the synthesized AEM comprised an easily degradable polymeric structure under a temperature of 80 °C, which is higher than the temperature of 60 °C corresponding to degradation of the cationic group and polymer backbone upon exposure to an aqueous base. In other words, it is necessary to examine the operating temperatures suitable for the AEM to achieve high and stable performance. AEMWEs with the FAA membrane at different operating temperatures are named FAA-MEA-Ts; likewise, AEMWEs with the Orion TM1™ membrane are named TM1-MEA-Ts, where T represents the operating temperatures of 50, 60, 70, and 80 °C. Fig. 2.3.7 presents the polarization curves of FAA-MEA-Ts and TM1-MEA-Ts. As shown in Fig. 2.3.7(a)-(d), the performance increased with the increase in the cell temperature at all voltage regions with FAA-MEA-Ts and TM1-MEA-Ts, as expected. This is attributed to the improvement in the ionic conductivity of AEM due to the high temperature, which agrees well with the findings of other published studies [14,36]. Notably, the TM1-MEA-Ts showed higher performance compared with the FAA-MEA-Ts at all operating temperatures. The current densities at 1.9 V_{cell} of TM1-MEA-50, -60, -70, and -80 were 292, 185, 171, and 158% higher than those of FAA-MEA-50, -60, -70, and -80, respectively. These results contributed to the higher ionic conductivity of the Orion TM1™ membrane compared to that of the FAA membrane. The FAA membrane consists of aminated polyarylene (polysulfone) chloride polymer, which contains ether bonds in the backbone [17]. However, aryl-ether, which is composed mostly of the AEM

structure, is considered to be decomposed by the ether hydrolysis mechanism at a high pH condition [37]. An especially unstable quinone methide structure produced from degraded polysulfone can lead to a decrease in the IEC due to the accelerated loss of anion exchange groups [38]. Thus, it is reported that the aryl-ether free structured AEM showed high durability [18,39,40]. The Orion TM1™ membrane is polyphenylene-based, i.e., it has an aryl-ether free and hydrophobic backbone structure [39]. This helps not only in maintaining the polymer structure with high ionic conductivity but also in preventing the attack of hydrophilic hydroxide ions [15]. Therefore, the Orion TM1™ membrane is considered a high and durable AEM for AEMWE.

To attain the optimized operating temperature, the effect of the operating temperatures on the stability of AEMWE using the Orion TM1™ membrane was investigated. As shown in Fig. 2.3.8, the degradation rates of TM1-MEAs operated under temperatures of 50, 60, 70, and 80 ^{o}C were approximately, 40, 47, 55, and 321 mV h^{-1}, respectively. That is, degradation increased with increasing temperature, indicating that high cell temperature can be susceptible to the degradation of the AEM. The cell temperature is optimized to achieve the trade-off between ion conductivity and stability. At higher temperatures, the ohmic resistance decreases and thereby the cell performance increases owing to the enhancement of ion conductivity; hydroxide ions can more easily move through a loosely packed polymer structure [41]. Simultaneously, the high temperature causes the degradation of the AEM and ionomer as hydroxide ions attack the backbone structure of the AEM, increasing the voltage rapidly [42]. Therefore, a temperature of 70 ^{o}C was confirmed to correspond to high performance and stability owing to the structural advantages of the Orion TM1™ membrane. The TM1-MEA-70 showed uniform hydrogen productivity during the stability test as indicated in Fig. 2.3.9.

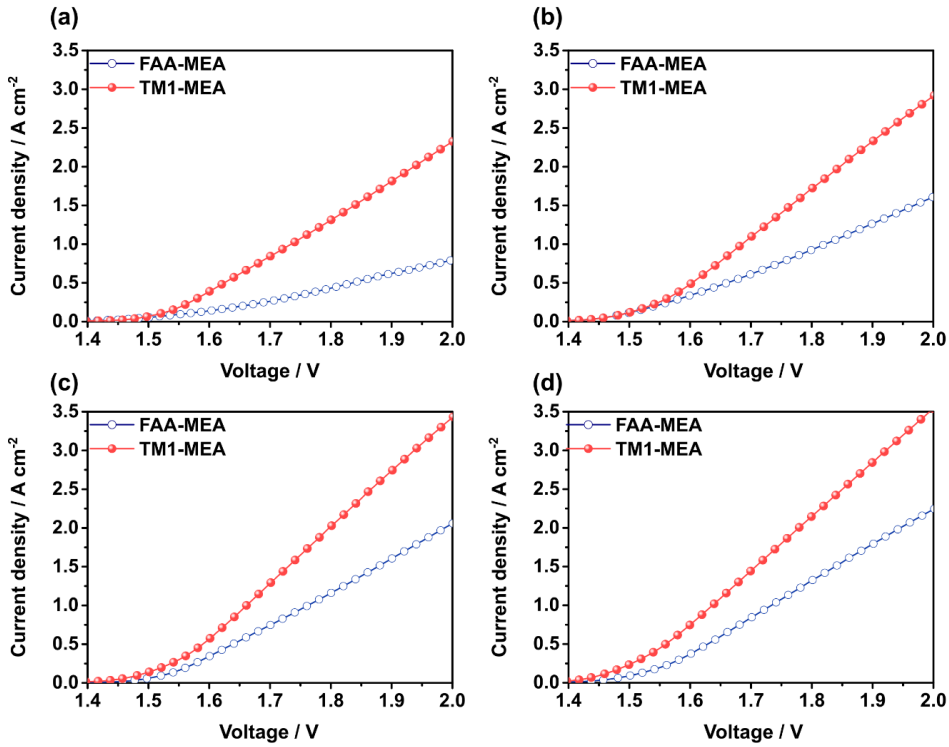

Figure 2.3.7 Polarization curves of AEMWEs (FAA-MEA-Ts and TM1-MEA-Ts for T: 50, 60, 70, and 80) operated under cell temperatures of (a) 50, (b) 60, (c) 70, and (d) 80 °C. The cathode and anode ionomer contents were fixed to 30 and 10 wt.%, respectively, and the cathode and anode catalyst loadings were constant at 0.4 mg_{Pt} cm^{-2} and 2 mg_{IrO2} cm^{-2}, respectively.

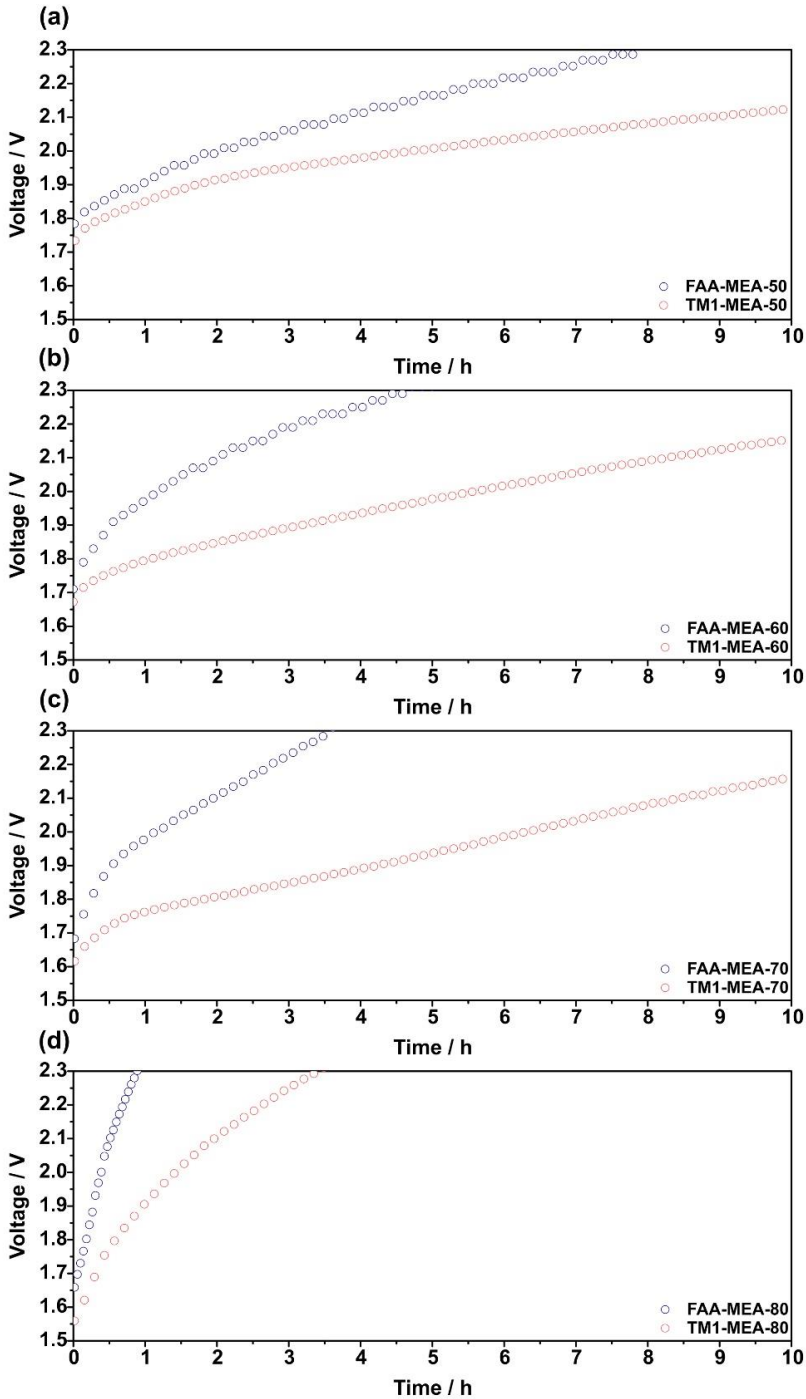

Figure 2.3.8 Stability tests of two AEMWEs (FAA-MEA-Ts and TM1-MEA-Ts (T: 50, 60, 70, and 80)) operated under cell temperatures of (a) 50, (b) 60, (c) 70, and (d) 80 ^{o}C at a constant current density of 500 mA cm^{-2}.

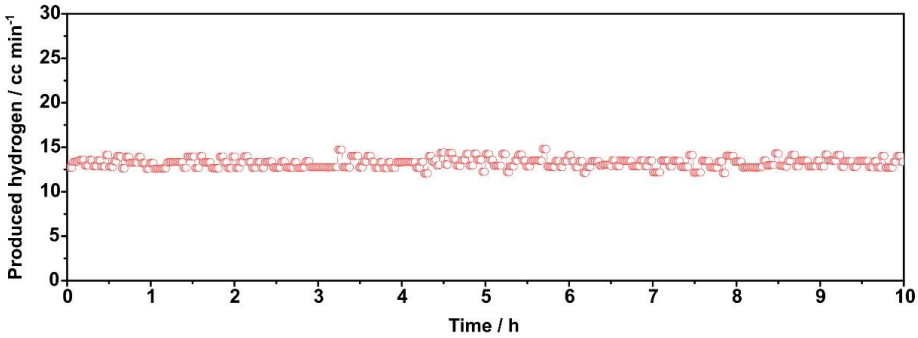

Figure 2.3.9 The amount of produced H_2 during stability test with Orion TM1™ membrane at a current density of 500 mA cm^{-2}. The cell temperature was maintained at 70 ºC and 1 M KOH was supplied to both electrodes.

Effect of reactants

To investigate the influence of the feeding solution, an AEMWE test was conducted by supplying pure water and alkaline solution of 1.0 M KOH to each electrode. The reactants fed to the anode/cathode are denoted by A/B. Four feeding conditions, i.e., KOH/KOH, water/KOH, KOH/water, and water/water, were used. As shown in Fig. 7, the performance of the TM1-MEA exceeded that of FAA-MEA under all feeding conditions, owing to the high ionic conductivity of the Orion TM1™ membrane. Under KOH/KOH, the TM1-MEA exhibited the highest current density (2.75 A cm^{-2}); the lowest current density was achieved under the water/water condition (0.18 A cm^{-2}) at 1.9 V_{cell} (Fig. 2.3.10(a), (d)). Interestingly, the TM1-MEA with KOH/water achieved comparable performance (1.43 A cm^{-2}) to that of the FAA-MEA with KOH/KOH (1.51 A cm^{-2}) at 1.9 V_{cell}. As illustrated in Fig. 2.2.1, hydroxide ions produced from the cathode are conducted to the anode through the AEM. However, the low ionic conductivity of the AEM induces an insufficient supply of hydroxide ions to the anode, directly influencing the performance of AEMWE. Various feeding conditions were employed to operate AEMWE, such as supplying alkaline solution to both electrodes [14] or to the anode only [36] and supplying pure water to both electrodes [42], only to the anode, or only to the cathode [33]. In most previous studies, higher performance was achieved with feeding high pH solution, such as KOH and NaOH rather than pure water [33,36,42-45], producing scant hydroxide ions. The use of water as a feeding solution led to relatively low performance, as indicated in Fig. 2.3.10. Although most AEMWE researches have been conducted under a feeding alkaline solution, the use of pure water should be pursued. This is because the AEMs soaked in the alkaline solution, even without any additional applied stress, underwent loss of IEC and physical strength within 1000 h [15,18,35]. The higher current density of the TM1-MEAs compared to that of the FAA-MEAs probably contributed to the structure of the polymers composing the AEMs. The polyaromatic polymer with an ether bonds structure has been reported to be decomposed into phenol, which is

acidic, and it is possible to neutralize the hydroxide of the ammonium functional groups [46]. After all, the TM1-MEA showed a 156% higher current density at 1.9 V_{cell} compared to the FAA-MEA (Fig. 2.3.10(d)), though AEMWE operating with pure water exhibited lower performance than the MEA operating with 1 M KOH. Those results suggest that the TM1-MEA shows potential when using a diluted alkaline solution or pure water.

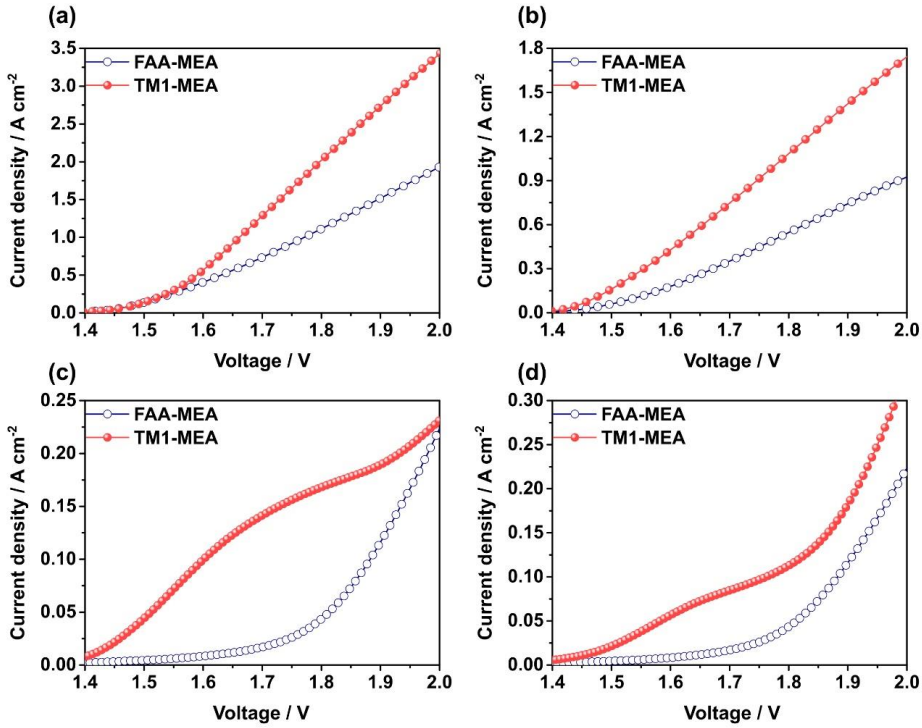

Figure 2.3.10 Polarization curves of two AEMWEs (FAA-MEA and TM1-MEA) operated with different feeding methods (anode/cathode): (a) KOH/KOH, (b) KOH/water, (c) water/KOH, and (d) water/water. The cell temperature was 70 ºC.

Performance and durability comparison of optimized MEA

The optimized TM1-MEA shows a high current density of 2.75 A cm^{-2} at 1.9 V_{cell} with a high stability of 55 mV hr^{-1}, benefiting from the superior structural advantages of the Orion-TM1™ membrane. Fig. 2.3.11(a) indicates current density at 1.9 V_{cell} from those reported in the literature for AEMWE, and these are approximate values calculated from the graph [11-14,34,45-47]. The detailed information including the catalyst materials, loading for the cathode and anode, membrane, operating temperature, and feeding conditions are given in Table S1. As shown in Fig. 2.3.11(a) and Table S1, we achieved the highest performance among the researches on the commercial AEMs. The potential cycling stability test with optimized condition was evaluated with FAA-MEA and TM1-MEA (Fig. 2.3.11(b, c)). The current density of TM1-MEA was decreased 32% after 200 cycle, while the FAA-MEA was decreased 85%, suggesting the definitely better stability of TM1-MEA. The two showed similar behavior that current density was rapidly decreased during first 100 cycles. As shown in Fig. 2.3.11(d), the voltage of TM1-MEA gradually increased to around 20 h and showed steady voltage profile till 50 h, while the voltage of FAA-MEA sharply rose to 2.3 V_{cell} in 3.4 h.

The performance developed in this work is the highest among the reports on commercial ionomeric anion-exchange membranes for AEMWE. Thus, the Orion TM1™ membrane can be considered as an ionomeric anion-exchange membranes for AEMWE.

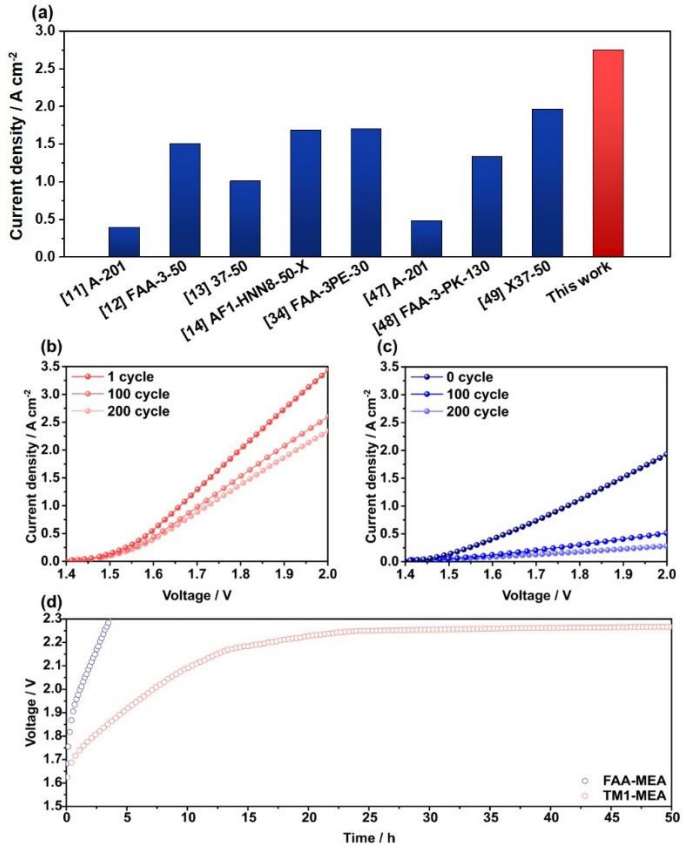

Figure 2.3.11 (a) Comparison with AEMWE performances obtained at 1.9 V as reported in literature [11-14,34,47-49] and developed in this work (70 ^{o}C). Polarization curves of AEMWEs after 100 and 200 cycles with (b) FAA-MEA and (c) TM1-MEA. (d) Stability tests of two AEMWE (FAA-MEA and TM1-MEA) under optimized conditions at a constant current density of 500 mA cm^{-2}.

2.4. Conclusion

High-performance and durable AEMWE was developed by using an aryl-ether free polyphenylene-based AEM. First, we optimized the electrode parameters, i.e., the ionomer content and catalyst loading, reducing the activation, ohmic, and mass transportation resistances. The performance of the TM1-MEA exceeded that of the FAA-MEA under all temperatures owing to the ionic conductivity of the AEM. In addition, the TM1-MEA showed a more stable voltage profile than the FAA-MEA at various operating temperatures. This is because the beneficial aryl-ether free structure and hydrophobic properties of the Orion-TM1 membrane inhibited decomposition by ether hydrolysis and access of hydrophilic hydroxide ions. The TM1-MEA also exhibited higher performance than the FAA-MEA for all feeding conditions, including the diluted alkaline solution and pure water condition, which is a less corrosive condition for AEMs. The optimal TM1-MEA showed a remarkably high AEMWE performance, which is notably higher than those reported in literature Thus, the Orion TM1^{TM} membrane can be considered as an alternative to conventional AEMs for high-performance and durable AEMWE.

2.5. References

[1] Guillet N, Millet P. Alkaline water electrolysis. Hydrogen Production. 2015:117-66.

[2] David M, Ocampo-Martínez C, Sánchez-Peña R. Advances in alkaline water electrolyzers: A review. Journal of Energy Storage. 2019;23:392-403.

[3] Carmo M, Fritz DL, Mergel J, Stolten D. A comprehensive review on PEM water electrolysis. International journal of hydrogen energy. 2013;38:4901-34.

[4] Kumar SS, Himabindu V. Hydrogen production by PEM water electrolysis–A review. Materials Science for Energy Technologies. 2019;2:442-54.

[5] Cho MK, Lim A, Lee SY, Kim H-J, Yoo SJ, Sung Y-E, et al. A Review on Membranes and Catalysts for Anion Exchange Membrane Water Electrolysis Single Cells. J Electrochem Sci Technol. 2017;8:183-96.

[6] Miller HA, Bouzek K, Hnat J, Loos S, Bernäcker CI, Weißgärber T, et al. Green hydrogen from anion exchange membrane water electrolysis: a review of recent developments in critical materials and operating conditions. Sustainable Energy & Fuels. 2020;4:2114-33.

[7] Chu Y, Chen Y, Chen N, Wang F, Zhu H. A new method for improving the ion conductivity of anion exchange membranes by using TiO 2 nanoparticles coated with ionic liquid. RSC advances. 2016;6:96768-77.

[8] You W, Padgett E, MacMillan SN, Muller DA, Coates GW. Highly conductive and chemically stable alkaline anion exchange membranes via ROMP of trans-cyclooctene derivatives. Proceedings of the National Academy of Sciences. 2019;116:9729-34.

[9] Pavel CC, Cecconi F, Emiliani C, Santiccioli S, Scaffidi A, Catanorchi S, et al. Highly efficient platinum group metal free based membrane-electrode assembly for

anion exchange membrane water electrolysis. Angewandte Chemie International Edition. 2014;53:1378-81.

[10] Cho MK, Park H-Y, Choe S, Yoo SJ, Kim JY, Kim H-J, et al. Factors in electrode fabrication for performance enhancement of anion exchange membrane water electrolysis. Journal of Power Sources. 2017;347:283-90.

[11] Vincent I, Kruger A, Bessarabov D. Development of efficient membrane electrode assembly for low cost hydrogen production by anion exchange membrane electrolysis. International Journal of Hydrogen Energy. 2017;42:10752-61.

[12] Park JE, Kang SY, Oh S-H, Kim JK, Lim MS, Ahn C-Y, et al. High-performance anion-exchange membrane water electrolysis. Electrochimica Acta. 2019;295:99-106.

[13] Liu Z, Sajjad SD, Gao Y, Yang H, Kaczur JJ, Masel RI. The effect of membrane on an alkaline water electrolyzer. International Journal of Hydrogen Energy. 2017;42:29661-5.

[14] Fortin P, Khoza T, Cao X, Martinsen SY, Barnett AO, Holdcroft S. High-performance alkaline water electrolysis using Aemion™ anion exchange membranes. Journal of Power Sources. 2020;451:227814.

[15] Meek KM, Antunes CM, Strasser D, Owczarczyk ZR, Neyerlin A, Pivovar BS. High-throughput anion exchange membrane characterization at NREL. ECS Transactions. 2019;92:723.

[16] Kim OH, Ahn CY, Kang SY, Kim S, Choi HJ, Cho YH, et al. From Half-Cells to Membrane-Electrode Assemblies: a Comparison of Oxygen Reduction Reaction Catalyst Performance Characteristics. Fuel Cells. 2019;19:695-707.

[17] Zarrin H, Wu J, Fowler M, Chen Z. High durable PEK-based anion exchange membrane for elevated temperature alkaline fuel cells. Journal of Membrane Science. 2012;394-395:193-201.

[18] Cha MS, Park JE, Kim S, Han S-H, Shin S-H, Yang SH, et al. Poly(carbazole)-based anion-conducting materials with high performance and durability for energy conversion devices. Energy & Environmental Science. 2020;13:3633-45.

[19] Carmo M, Doubek G, Sekol RC, Linardi M, Taylor AD. Development and electrochemical studies of membrane electrode assemblies for polymer electrolyte alkaline fuel cells using FAA membrane and ionomer. Journal of Power Sources. 2013;230:169-75.

[20] Al Lafi AG. FTIR spectroscopic analysis of ion irradiated poly (ether ether ketone). Polymer degradation and stability. 2014;105:122-33.

[21] Olvera LI, Guzmán-Gutiérrez MT, Zolotukhin MG, Fomine S, Cárdenas J, Ruiz-Trevino FA, et al. Novel high molecular weight aromatic fluorinated polymers from one-pot, metal-free step polymerizations. Macromolecules. 2013;46:7245-56.

[22] Faid AY, Xie L, Barnett AO, Seland F, Kirk D, Sunde S. Effect of anion exchange ionomer content on electrode performance in AEM water electrolysis. International Journal of Hydrogen Energy. 2020;45:28272-84.

[23] Xu W, Scott K. The effects of ionomer content on PEM water electrolyser membrane electrode assembly performance. International Journal of Hydrogen Energy. 2010;35:12029-37.

[24] Hegge F, Moroni R, Trinke P, Bensmann B, Hanke-Rauschenbach R, Thiele S, et al. Three-dimensional microstructure analysis of a polymer electrolyte membrane water electrolyzer anode. Journal of Power Sources. 2018;393:62-6.

[25] Su H, Linkov V, Bladergroen BJ. Membrane electrode assemblies with low noble metal loadings for hydrogen production from solid polymer electrolyte water electrolysis. International Journal of Hydrogen Energy. 2013;38:9601-8.

[26] Springer T, Zawodzinski T, Wilson M, Gottesfeld S. Characterization of polymer electrolyte fuel cells using AC impedance spectroscopy. Journal of the Electrochemical Society. 1996;143:587.

[27] Kinoshita K. Carbon: electrochemical and physicochemical properties. 1988.

[28] Reiser CA, Bregoli L, Patterson TW, Yi JS, Yang JD, Perry ML, et al. A Reverse-Current Decay Mechanism for Fuel Cells. Electrochemical and Solid-State Letters. 2005;8.

[29] Ahn C-Y, Kang SY, Choi HJ, Kim O-H, Sung Y-E, Cho Y-H. Effect of anode iridium oxide content on the electrochemical performance and resistance to cell reversal potential of polymer electrolyte membrane fuel cells. International Journal of Hydrogen Energy. 2021;46:14713-23.

[30] Ahn C-Y, Ahn J, Kang SY, Kim O-H, Lee DW, Lee JH, et al. Enhancement of service life of polymer electrolyte fuel cells through application of nanodispersed ionomer. Science advances. 2020;6:eaaw0870.

[31] Yu H, Roller JM, Mustain WE, Maric R. Influence of the ionomer/carbon ratio for low-Pt loading catalyst layer prepared by reactive spray deposition technology. Journal of Power Sources. 2015;283:84-94.

[32] Lettenmeier P, Kolb S, Sata N, Fallisch A, Zielke L, Thiele S, et al. Comprehensive investigation of novel pore-graded gas diffusion layers for high-performance and cost-effective proton exchange membrane electrolyzers. Energy & Environmental Science. 2017;10:2521-33.

[33] Leng Y, Chen G, Mendoza AJ, Tighe TB, Hickner MA, Wang CY. Solid-state water electrolysis with an alkaline membrane. J Am Chem Soc. 2012;134:9054-7.

[34] Cossar E, Oyarce Barnett A, Seland F, Baranova EA. The Performance of Nickel and Nickel-Iron Catalysts Evaluated As Anodes in Anion Exchange Membrane Water Electrolysis. Catalysts. 2019;9.

[35] Chen D, Hickner MA. Degradation of imidazolium- and quaternary ammonium-functionalized poly(fluorenyl ether ketone sulfone) anion exchange membranes. ACS Appl Mater Interfaces. 2012;4:5775-81.

[36] Lim A, Kim H-j, Henkensmeier D, Jong Yoo S, Young Kim J, Young Lee S, et al. A study on electrode fabrication and operation variables affecting the performance of anion exchange membrane water electrolysis. Journal of Industrial and Engineering Chemistry. 2019;76:410-8.

[37] Mohanty AD, Tignor SE, Krause JA, Choe Y-K, Bae C. Systematic Alkaline Stability Study of Polymer Backbones for Anion Exchange Membrane Applications. Macromolecules. 2016;49:3361-72.

[38] Miyanishi S, Yamaguchi T. Ether cleavage-triggered degradation of benzyl alkylammonium cations for polyethersulfone anion exchange membranes. Phys Chem Chem Phys. 2016;18:12009-23.

[39] Lee W-H, Park EJ, Han J, Shin DW, Kim YS, Bae C. Poly(terphenylene) Anion Exchange Membranes: The Effect of Backbone Structure on Morphology and Membrane Property. ACS Macro Letters. 2017;6:566-70.

[40] Yang Z, Guo R, Malpass-Evans R, Carta M, McKeown NB, Guiver MD, et al. Highly conductive anion-exchange membranes from microporous Tröger's base polymers. Angewandte Chemie. 2016;128:11671-4.

[41] Vincent I, Lee EC, Kim HM. Comprehensive impedance investigation of low-cost anion exchange membrane electrolysis for large-scale hydrogen production. Sci Rep. 2021;11:293.

[42] Li D, Park EJ, Zhu W, Shi Q, Zhou Y, Tian H, et al. Highly quaternized polystyrene ionomers for high performance anion exchange membrane water electrolysers. Nature Energy. 2020;5:378-85.

[43] Parrondo J, Arges CG, Niedzwiecki M, Anderson EB, Ayers KE, Ramani V. Degradation of anion exchange membranes used for hydrogen production by ultrapure water electrolysis. RSC Advances. 2014;4.

[44] Xiao L, Zhang S, Pan J, Yang C, He M, Zhuang L, et al. First implementation of alkaline polymer electrolyte water electrolysis working only with pure water. Energy & Environmental Science. 2012;5.

[45] Park EJ, Capuano CB, Ayers KE, Bae C. Chemically durable polymer electrolytes for solid-state alkaline water electrolysis. Journal of Power Sources. 2018;375:367-72.

[46] Li D, Matanovic I, Lee AS, Park EJ, Fujimoto C, Chung HT, et al. Phenyl oxidation impacts the durability of alkaline membrane water electrolyzer. ACS applied materials & interfaces. 2019;11:9696-701.

[47] Pavel CC, Cecconi F, Emiliani C, Santiccioli S, Scaffidi A, Catanorchi S, et al. Highly efficient platinum group metal free based membrane-electrode assembly for anion exchange membrane water electrolysis. Angew Chem Int Ed Engl. 2014;53:1378-81.

[48] Thangavel P, Ha M, Kumaraguru S, Meena A, Singh AN, Harzandi AM, et al. Graphene-nanoplatelets-supported NiFe-MOF: high-efficiency and ultra-stable oxygen electrodes for sustained alkaline anion exchange membrane water electrolysis. Energy & Environmental Science. 2020;13:3447-58.

[49] Jang MJ, Yang J, Lee J, Park YS, Jeong J, Park SM, et al. Superior performance and stability of anion exchange membrane water electrolysis: pH-controlled copper cobalt oxide nanoparticles for the oxygen evolution reaction. Journal of Materials Chemistry A. 2020;8:4290-9.

Chapter 3. The design of porous structure via one-step process for anion exchange membrane water electrolyzer

3.1. Introduction

Hydrogen is a rising energy resource to alter fossil fuels owing to its beneficial properties such as high energy density and zero-emission [1]. To keep up with the demand for hydrogen, a water electrolyzer has been attracted to produce sustainable and high purity of hydrogen [2, 3]. Among various types of water electrolyzers, an anion-exchange membrane water electrolyzer (AEMWE) has been considered as a promising water electrolyzer. AEMWEs use an anion-exchange membrane (AEM) as an electrolyte so that a higher efficiency could be obtained by this zero-gap design compared to an alkaline water electrolyzer that employs alkaline solution as an electrolyte. Another great advantage of AEMWE is the use of non-PGM electrocatalysts [4, 5] since the electrochemical reactions occur in alkaline condition. Meanwhile, the electrodes for proton exchange membrane water electrolyzer (PEMWE) requires platinum-group metals (PGMs) such as Ir, Ru and Pt since PEMWE is operated under highly corrosive acidic condition [6].

For polymer electrolyte membrane-based electrochemical devices including water electrolyzers and fuel cells, catalyst slurry-based processes (i.e. spraying, screen printing, and doctor blading), and the catalyst slurry includes catalyst particle, ionomer and solvent, have been employed in the fabrication of membrane-electrode assembly (MEA)[5, 7]. The ionomer, often involved in slurry-based processes, improves the single-cell performance by increasing the ion transport pathway in the catalyst layer and gives mechanical support by binding each catalyst particle. However, the ionomer is known to be degraded during the AEMWE operation [8], and the low stability of the ionomer is a significant disadvantage to

the AEMWE because the degraded ionomer reduces the triple-phase boundary, which occurs in actual electrochemical reaction [9, 10].

Electro-deposition (ED) is one of the fabrication processes for electrochemical devices since it is facile, reproducible, and scalable with simple equipment [11]. Several studies have reported that electrodes prepared with ED. Park et al. fabricated a uniform thin film NiFeOOH on SUS felt using ED with high OER activity and durability [12]. Zhang et al. prepared a film-like Ni-Fe electrocatalyst on Ni foam for HER electrode [13]. However, most of the electrodes fabricated with ED were two-dimensional shaped electrodes, which may have lower ECSA than three-dimensional porous electrode. The composite material electrode with two metal species could also be fabricated ED (co-ED) when the targeted metal ions, included in the ED solution, have similar reduction potentials.

The porous catalyst layer structure has been considered as an effective strategy that enhances the mass transfer of reactant and product as well as improves active sites by increasing specific surface area. Several strategies have been adopted to develop a porous structured catalyst layer, including the three-dimensionally ordered inverse-opal structure[14], the hollow core-mesoporous shell carbons [15], the metal oxide clusters using aerosol synthesis [16], and the carbon nanofiber or carbon nanotube supported catalyst [17,18]. However, the porous catalyst layer fabrication often involves several steps of procedures, which increase the process cost.

In this work, the ionomer-free and porous NiFe electrode on Ni foam (p-NiFe@NF) using a facile one-step electrodeposition process was proposed as anode for AEMWE. The three-dimensionally porous structure electrode offers improved active sites and mass transfer by controlling applying current during ED without additional process. The high electronic conductivity and durability was obtained with the ionomer-free electrode. The 3D p-NiFe@NF is directly

employed as porous transport layer and catalyst layer with superior AEMWE performance and durability.

3.2. Experimental

Fabrication of the anode electrode

The NiFe was directly coated on Ni foam using a one-step ED process. Prior to ED of NiFe on Ni foam, Ni foam (Alantum, Republic of Korea) with 1600 μm thickness was pressed to 350 μm. For the preparation of electrolyte solution for ED, nickel nitrate hexahydrate ($Ni(NO_3)_2 \cdot 6H_2O$, Sigma Aldrich, USA), iron nitrate nonahydrate ($Fe(NO_3)_3 \cdot 9H_2O$, Sigma Aldrich, USA), boric acid (H_3BO_3, Sigma Aldrich, USA) were dissolved in de-ionized (DI) water and the mixture were well stirred for more than 2 h. The molar ratio of Ni and Fe precursor were 1:1. ED was performed with the standard three-electrode system. The pressed Ni foam, platinum mesh and Ag/AgCl were employed as working, counter and reference electrode, respectively. The distance between the three electrodes was kept constant during the ED process to maintain the ohmic resistance. To deposit NiFe on Ni foam, -50 mA cm^{-2} of current was applied to the working electrode using an electrochemical workstation (PGSTAT302N, Metrohm, Switzerland) for 600 s at room temperature. The fabricated with simple direct current ED process was denoted as e-NiFe@NF. To fabricate porous NiFe on Ni foam (p-NiFe@NF), the pulse-current method was adopted. -50 and 0 mA cm^{-2} of current was repeatably applied for 600 cycles, and the on/off time ratio was 1. All the samples prepared with ED were rinsed with DI water and dried at 80 ^oC in a vacuum chamber overnight. The mass of e-NiFe and p-NiFe deposited on Ni foam was calculated to be about 0.3 mg cm^{-2}. For reference, commercial iron-nickel alloy particles (Sigma Aldrich, USA) were sprayed on the Ni foam (c-NiFe@NF). The ink solution composed of commercial iron-nickel alloy particles (Sigma-Aldrich, USA), 2-propanol (Sigma-Aldrich, USA), and DI water was sprayed on Ni foam with an air spraying gun.

Physicochemical characterization

The crystallinity of each sample was investigated by X-ray diffraction (XRD; smartlab, Rigaku, Japan) equipped with a Cu target at 40 kV and 30 mA, with a scan rate of 2^{o} min^{-1} in the 2θ range from 20 to 80^{o}. The elemental composition and chemical states of catalysts were analyzed by X-ray photoelectron spectroscopy (XPS; Sigma Probe, Thermo VG Scientific, USA) with monochromatic Al Kα source. The morphologies and compositions were characterized with transmission electron microscopy (TEM; JEOL, Japan), element mapping analysis and energy-dispersive X-ray spectroscopy (EDS; JEOL, Japan). The morphologies of c-NiFe@NF, e-NiFe@NF, and p-NiFe@NF were characterized using a field emission scanning electron microscope (FE-SEM, SUPRA, Carl Zeiss, Germany) with 2 kV of accelerating voltage. A focused ion beam (FIB, AURIGA, Carl Zeiss, Germany) was adopted to characterizing the cross-section of fabricated catalyst layer on Ni foam. To measure the pore size distribution and porosity of electrodes, a mercury intrusion porosimeter (PM33GT, Quantachrome, USA) was used.

Fabrication of MEA

The membrane electrode assembly (MEA) was prepared by sandwiching an FAA-3 as an anion-exchange membrane (Fumatech, Germany) between the anode catalyst on Ni foam and the cathode. For the cathode, the mixture of 40 wt.% Pt/C particles (Johnson Matthey, USA) and FAA-3-Br ionomer (Fumatech, Germany) in IPA, DI water was sprayed on carbon paper with microporous layer (JNT-40-A3, JNTG, Republic of Korea) used as cathode porous transport layer (PTL) and the catalyst loading was fixed at 0.4 mg_{Pt} cm^{-2}. The active area of the anode and cathode was 5 cm^{2}.

Electrochemical characterization

The single-cell test was performed with the AEMWE test station (CNL Energy, Republic of Korea). Pre-heated 1 M KOH solution (SAMCHUN, Republic of Korea) at a temperature of 60 ^{o}C was supplied into the both anode and cathode with constant flow rates of 5 mL min^{-1}. The single-cell temperature was maintained at 60 ^{o}C during the performance test. The polarization curves were obtained using the linear sweep method in a range of 1.35 to 2.05 V_{RHE}. with a scan rate of 5 mV s^{-1}. For the electrochemical impedance spectroscopy (EIS), a constant current of 1 A cm^{-2} over the frequency range of 0.1 Hz to 100 kHz was applied with the same feeding condition temperature of the single-cell operation. The stability of the AEMWE was measured with the chronoamperometry method at a current density of 1.0 A cm^{-2}. The electrochemical active area (ECSA) of e-NiFe@NF and p-NiFe@NF electrode was assumed with the double layer capacitance (C_{dl}) using cyclic voltammetry (CV) at scan rates from 10 to 120 mV s^{-1} in the range of 0.2 to 0.3 V in the two-electrode system, by using the cathode as a counter and reference electrode.

3.3. Results and discussion

X-ray photoelectron spectroscopy (XPS) was conducted to investigate the surface chemical composition and elemental valence states in the sample. The wide scan XPS survey spectra in Fig. 3.3.1(a) obviously shows the presence of Ni, Fe, C and O elements. The high-resolution XPS Ni 2p spectra shown in Fig. 3.3.1(b) exhibits two main peaks located at 854.7 and 860.6 eV are attributed to Ni^{2+} $2p_{3/2}$ and Ni^{2+} $2p_{1/2}$, respectively [19]. In the Fe 2p spectra indicated in Fig. 3.3.1(c) exhibits the doublet at 710.8 eV for Fe $2p_{3/2}$ and 723.8 eV for Fe $2p_{1/2}$, indicating the presence of Fe^{2+} in e-NiFe@NF [20]. Fig. 3a, b shows the TEM images of c-NiFe particles (Fig. 3.3.2(a)) and e-NiFe (Fig. 3.3.2(b)). The commercial NiFe particles showed irregular shape and size distribution. Meanwhile, the synthesized NiFe showed a sheet-like shape as it was obtained by scratching from e-NiFe@NF.

To evaluate the single-cell performance, the e-NiFe@NF anode was used to fabricate the MEA, and as a reference, MEA with c-NiFe was employed. From Fig. 3.3.3(a), the MEA with e-NiFe@NF exhibited an outstanding performance for AEMWE, which had obviously a higher current density of 2.82 A cm^{-2} while the conventional MEA showed 1.79 A cm^{-2} at 1.9 V_{cell}, indicating the higher performance of e-NiFe toward OER. The low ohmic resistance of MEA with e-NiFe@NF was also confirmed with Nyquist plot shown in Fig. 3.3.3(b). In the Nyquist plot, the intersection at x-axis on high frequency is related to the ohmic resistance attributed from ionic and electronic transfer. The ionomer included in MEA with c-NiFe@NF may improve the ionic mobility between AEM and active site on the surface of electrocatalyst, the much lower electron conductivity caused the higher ohmic resistance of the MEA with c-NiFe@NF than the MEA with e-NiFe@NF. Thus, this superior performance of e-NiFe@NF is mainly derived from the high catalytic activity of e-NiFe and ionomer-free catalyst layer.

Fig. 3.3.4 shows the cross-section images of e-NiFe@NF and p-NiFe@NF using FIB. As observed, the p-NiFe@NF exhibits dense structure up to 1 μm; above 1 μm, the pores increase, while e-NiFe@NF shows dense formation without distinct pores. The total thickness of p-NiFe@NF and e-NiFe@NF was about 2.0 μm and 1.4 μm, respectively. The thicker catalyst layer of p-NiFe@NF is attributed to the porous structure even same loading (~ 0.3 mg cm^{-2}) with e-NiFe@NF. This distinct morphology of p-NiFe@NF was associated with the ED process. The film formation of metals using ED follows the three steps: nucleation, growth, film formation [21]. When the e-NiFe@NF is prepared using direct current process, as shown in Fig. 3.3.5(a), potential rapidly decrease from 0 to -2.9 $V_{Ag/AgCl}$ during the first 50 s, which is region of nucleation on the surface of Ni foam. Between 50 and 600 s which exhibits relatively stable potential profile, the NiFe film was grew up on the nuclear. With the pulse current process, however, the potential dynamically changed as the repeated applied current. After 600 s, the potential was gradually increased to – 2.1 $V_{Ag/AgCl}$, which could be generate small hydrogen bubbles on the working electrode. The pores on p-NiFe@NF are attributed to those small hydrogen bubbles that could not be removed on the surface because those are too small to detached from the surface on the Ni foam.

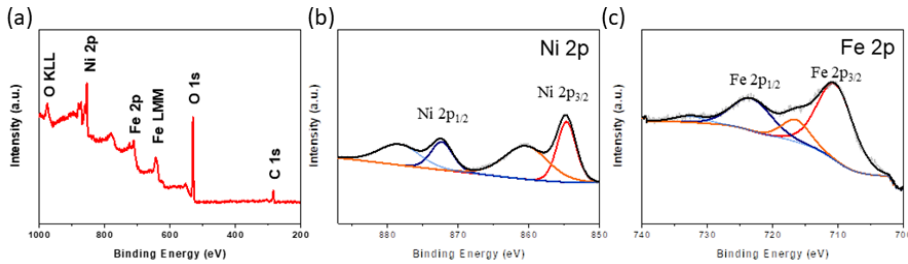

Figure 3.3.1 (a) XPS survey spectrum of e-NiFe@NF and the corresponding high-resolution XPS spectra of (b) Ni 2p, (c) Fe 2p.

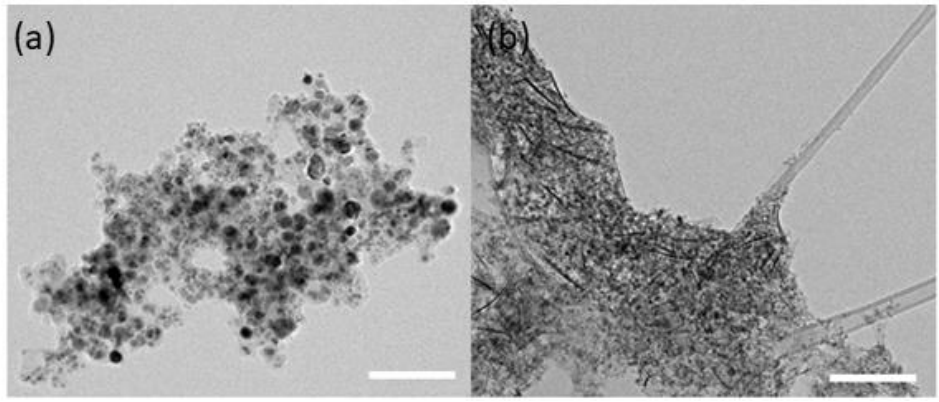

Figure 3.3.2 TEM images of (a) c-NiFe and (b) e-NiFe scratched off from the e-NiFe@NF. Scale bar represents 100 nm.

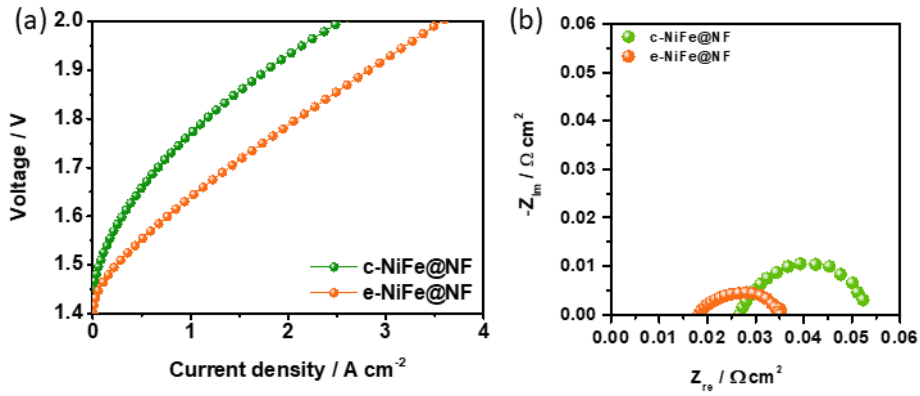

Figure 3.3.3 (a) Polarization curves and (b) Nyquist plots in the e-NiFe@NF MEA and c-NiFe@NF MEA. The catalyst loading for anode is 0.3 mg cm^{-2}

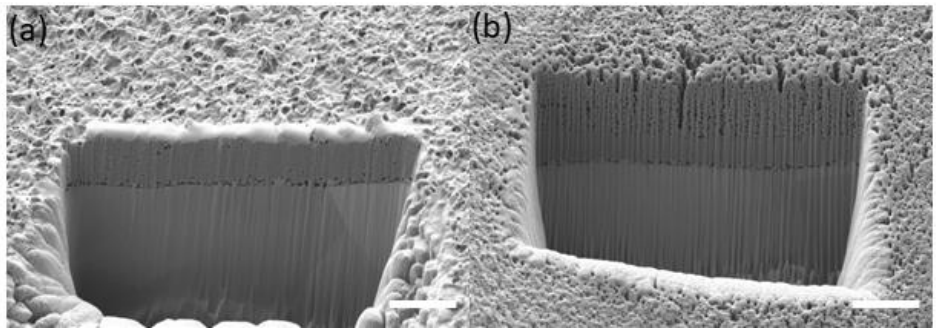

Figure 3.3.4 FE-SEM images of (a) e-NiFe@NF and (b) p-NiFe@NF. The scale bars represent 2 μm.

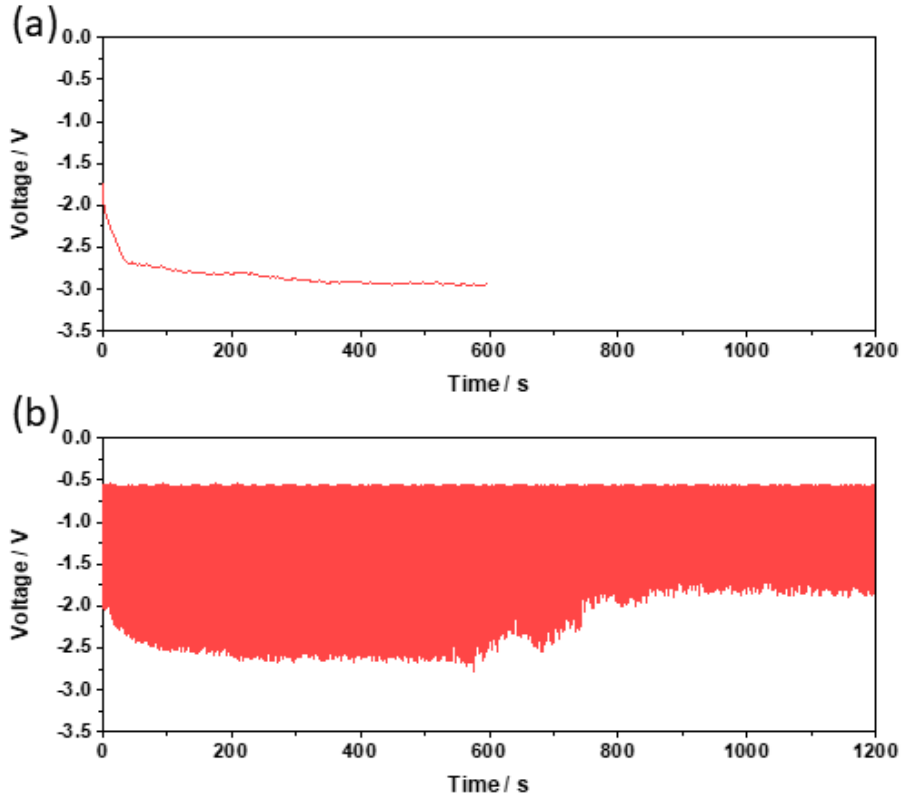

Figure 3.3.5 Voltage profile during the fabrication of (a) e-NiFe@NF and (b) p-NiFe@NF

Fig. 3.3.6(a) shows the polarization curves of MEA with e-NiFe@NF and p-NiFe@NF. The performance of MEA with p-NiFe@NF is significantly higher than that of MEA with NiFe@NF, indicating a current density of 3.87 A cm^{-2} at 1.9 V. The advantage of novel structured p-NiFe@NF was also verified by EIS analysis. The EIS analysis was conducted at constant current mode at different current density. To observe catalytic kinetics, EIS analysis was conducted at 0.1 A cm^{-2} and 1 A cm^{-2} to observe catalytic kinetics and mass transfer, respectively. The smaller diameter of semicircle of MEA with p-NiFe@NF in the Nyquist plot at 0.1 A cm^{-2} is may attributed to higher active sites due to the large interface area between the reactant and the surface of catalyst layer owing to the porous electrode morphology. Moreover, the MEA with p-NiFe@NF showed smaller semicircle at 1.0 A cm^{-2} as well, implying improved mass transfer [22], since the porous structure of p-NiFe@NF facilitates the access of reactant to the active sites. In addition, the electrochemical active area (ECSA) of the p-NiFe@NF and e-NiFe@NF were estimated from double-layer capacitance (C_{dl}), which obtained from cyclic voltammetry (CV) at non-faradaic region with various scan rate. The C_{dl} of p-NiFe@NF was 21 mF cm^{-2} while NiFe@NF was 6 mF cm^{-2}. We found that the p-NiFe@NF has a higher ECSA than e-NiFe@NF, suggesting that the p-NiFe@NF have more active sites owing to the porous structure than e-NiFe@NF. This novel structure in p-NiFe@NF greatly influenced to performance of AEMWE by enhancing catalytic kinetics and mass transfer. To examine the durability of the MEAs with c-NiFe@NF and p-NiFe@NF, chronopotentiometry at an applied current density of 1 A cm^{-2} was used for 100 h. As shown in Fig. 3.3.7, the potential of MEA with c-NiFe@NF rapidly increased in 100 h, showing 11.2 mV h^{-1} of potential increasing rate. In contrast, the potential gap of MEA with p-NiFe@NF between before and after 100 h exhibited remarkably lower value than that of c-NiFe@NF under same operating conditions. The lower electrode durability of c-NiFe@NF may be attributed to the low durability of ionomer contained in the catalyst layer. The binding strength of ionomer in the c-NiFe@NF is weak to

support the particles, resulting in the detachment of catalyst from the c-NiFe@NF electrode under circulation of feeding solution [23]. Moreover, the contained ionomer accelerates the degradation of AEMWE due to the decomposition of ionomers in the catalyst layer. Overall, the high performance and durability of p-NiFe@NF are mainly contributed to the following factors: (1) low ohmic resistance owing to the absence of non-electronic conductive ionomer, (2) enhanced mass transfer owing to the highly porous catalyst layer structure.

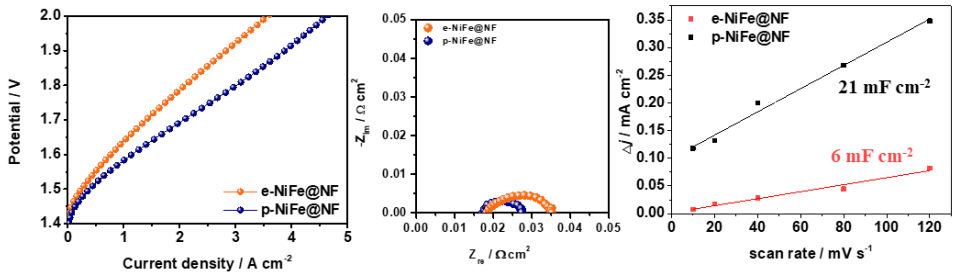

Figure 3.3.6 (a) The capacitive currents *vs.* scan rate of e-NiFe@NF MEA and p-NiFe@NF MEA. The linear slope is corresponded to the double-layer capacitance (C_{dl}) (b) Polarization curves and (b) Nyquist plots in the e-NiFe@NF MEA and p-NiFe@NF MEA. The catalyst loading for anode is 0.3 mg cm^{-2}. The Nyquist plots were obtained at 1.0 A cm^{-2}.

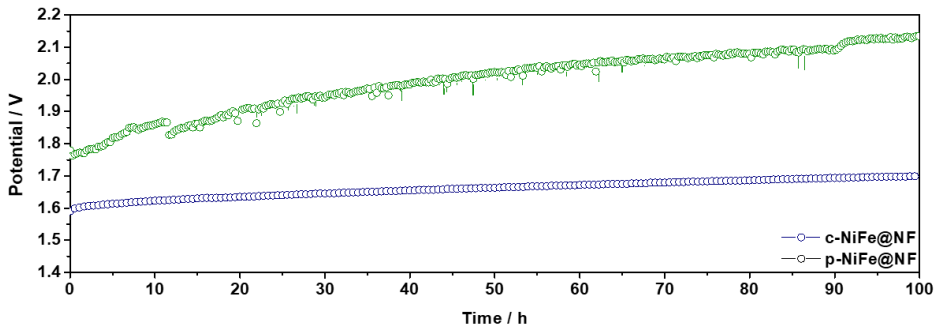

Figure 3.3.7 Durability test of AEMWEs with c-NiFe@NF, e-NiFe@NF, and p-NiFe@NF at a constant current density of 1 A cm^{-2}.

3.4. Conclusion

We developed the three-dimensional porous electrode without ionomer by only inducing off time during the ED process. The three-dimensional porous structure offered two advantages. First, high catalyst utilization was obtained by enlarging the specific surface area of catalyst layer. Secondly, enhanced mass transfer could be achieved by the macropores in the catalyst layer. The ionomer-free composition showed low ohmic resistance due to the absence of non-electronic conductive ionomer. Moreover, it prevented the degradation of electrode. These merits contribute to the outstanding performance (3.87 A cm^{-2} at 1.9 V_{cell}) and durability (increasing potential rate of 11.1 mV h^{-1}) for AEMWE.

3.5. References

[1] A.M. Abdalla, S. Hossain, O.B. Nisfindy, A.T. Azad, M. Dawood, A.K. Azad, Hydrogen production, storage, transportation and key challenges with applications: A review, Energy Conversion and Management, 165 (2018) 602-627.

[2] R. Abbasi, B.P. Setzler, S. Lin, J. Wang, Y. Zhao, H. Xu, B. Pivovar, B. Tian, X. Chen, G. Wu, Y. Yan, A Roadmap to Low-Cost Hydrogen with Hydroxide Exchange Membrane Electrolyzers, Adv Mater, 31 (2019) e1805876.

[3] X. Jia, Y. Zhao, G. Chen, L. Shang, R. Shi, X. Kang, G.I.N. Waterhouse, L.-Z. Wu, C.-H. Tung, T. Zhang, Ni3FeN Nanoparticles Derived from Ultrathin NiFe-Layered Double Hydroxide Nanosheets: An Efficient Overall Water Splitting Electrocatalyst, Advanced Energy Materials, 6 (2016).

[4] J.R. Varcoe, P. Atanassov, D.R. Dekel, A.M. Herring, M.A. Hickner, P.A. Kohl, A.R. Kucernak, W.E. Mustain, K. Nijmeijer, K. Scott, T. Xu, L. Zhuang, Anion-exchange membranes in electrochemical energy systems, Energy Environ. Sci., 7 (2014) 3135-3191.

[5] J.E. Park, S.Y. Kang, S.-H. Oh, J.K. Kim, M.S. Lim, C.-Y. Ahn, Y.-H. Cho, Y.-E. Sung, High-performance anion-exchange membrane water electrolysis, Electrochimica Acta, 295 (2019) 99-106.

[6] J.E. Park, J. Kim, J. Han, K. Kim, S. Park, S. Kim, H.S. Park, Y.-H. Cho, J.-C. Lee, Y.-E. Sung, High-performance proton-exchange membrane water electrolysis using a sulfonated poly(arylene ether sulfone) membrane and ionomer, Journal of Membrane Science, 620 (2021).

[7] M. Choi, J.K. Kim, J. Kim, S. Yang, J.E. Park, O.H. Kim, Y.H. Cho, PtRu/C catalyst slurry preparation for large-scale decal transfer with high performance of proton exchange membrane fuel cells, RSC Adv, 8 (2018) 36313-36322.

[8] D. Li, A.R. Motz, C. Bae, C. Fujimoto, G. Yang, F.-Y. Zhang, K.E. Ayers, Y.S. Kim, Durability of anion exchange membrane water electrolyzers, Energy & Environmental Science, 14 (2021) 3393-3419.

[9] E. López-Fernández, C. Gómez-Sacedón, J. Gil-Rostra, J.P. Espinós, A.R. González-Elipe, F. Yubero, A. de Lucas-Consuegra, Ionomer-Free Nickel-Iron bimetallic electrodes for efficient anion exchange membrane water electrolysis, Chemical Engineering Journal, 433 (2022).

[10] B. Pollet, A.A. Franco, H. Su, H. Liang, S. Pasupathi, Proton exchange membrane fuel cells, Compendium of Hydrogen Energy, Elsevier2016, pp. 3-56.

[11] X. Lu, C. Zhao, Electrodeposition of hierarchically structured three-dimensional nickel-iron electrodes for efficient oxygen evolution at high current densities, Nat Commun, 6 (2015) 6616.

[12] J.E. Park, S. Park, M.-J. Kim, H. Shin, S.Y. Kang, Y.-H. Cho, Y.-E. Sung, Three-Dimensional Unified Electrode Design Using a NiFeOOH Catalyst for Superior Performance and Durable Anion-Exchange Membrane Water Electrolyzers, ACS Catalysis, 12 (2021) 135-145.

[13] Z. Zhang, Y. Wu, D. Zhang, Potentiostatic electrodeposition of cost-effective and efficient Ni–Fe electrocatalysts on Ni foam for the alkaline hydrogen evolution reaction, International Journal of Hydrogen Energy, 47 (2022) 1425-1434.

[14] O.H. Kim, Y.H. Cho, S.H. Kang, H.Y. Park, M. Kim, J.W. Lim, D.Y. Chung, M.J. Lee, H. Choe, Y.E. Sung, Ordered macroporous platinum electrode and enhanced mass transfer in fuel cells using inverse opal structure, Nat Commun, 4 (2013) 2473.

[15] B. Fang, J.H. Kim, M.-S. Kim, J.-S. Yu, Hierarchical Nanostructuerd Carbons with Mes0-Macroporosity: Design, Characterization, and Application, Account of Chemical Research, 46 (2013) 1397-1406.

[16] M. Elmaalouf, M. Odziomek, S. Duran, M. Gayrard, M. Bahri, C. Tard, A. Zitolo, B. Lassalle-Kaiser, J.Y. Piquemal, O. Ersen, C. Boissiere, C. Sanchez, M. Giraud, M. Faustini, J. Peron, The origin of the high electrochemical activity of pseudo-amorphous iridium oxides, Nat Commun, 12 (2021) 3935.

[17] J.E. Park, M.-J. Kim, M.S. Lim, S.Y. Kang, J.K. Kim, S.-H. Oh, M. Her, Y.-H. Cho, Y.-E. Sung, Graphitic carbon nitride-carbon nanofiber as oxygen catalyst in anion-exchange membrane water electrolyzer and rechargeable metal–air cells, Applied Catalysis B: Environmental, 237 (2018) 140-148.

[18] N.M. Briggs, L. Barrett, E.C. Wegener, L.V. Herrera, L.A. Gomez, J.T. Miller, S.P. Crossley, Identification of active sites on supported metal catalysts with carbon nanotube hydrogen highways, Nat Commun, 9 (2018) 3827.

[19] A. Cano, I. Monroy, M. Ávila, D. Velasco-Arias, J. Rodríguez-Hernández, E. Reguera, Relevant electronic interactions related to the coordination chemistry of tetracyanometallates. An XPS study, New Journal of Chemistry, 43 (2019) 18384-18393.

[20] Y. Li, H. Zhang, M. Jiang, Q. Zhang, P. He, X. Sun, 3D Self-Supported Fe-Doped Ni2

P Nanosheet Arrays as Bifunctional Catalysts for Overall Water Splitting, Advanced Functional Materials, 27 (2017).

[21] S. Wang, X. Yin, D. Liu, Y. Liu, X. Qin, W. Wang, R. Zhao, X. Zeng, B. Li, Nanoscale observation of the solid electrolyte interface and lithium dendrite nucleation–growth process during the initial lithium electrodeposition, Journal of Materials Chemistry A, 8 (2020) 18348-18357.

[22] S. Sun, Z. Shao, H. Yu, G. Li, B. Yi, Investigations on degradation of the long-term proton exchange membrane water electrolysis stack, Journal of Power Sources, 267 (2014) 515-520.

[23] D. Li, E.J. Park, W. Zhu, Q. Shi, Y. Zhou, H. Tian, Y. Lin, A. Serov, B. Zulevi, E.D. Baca, C. Fujimoto, H.T. Chung, Y.S. Kim, Highly quaternized polystyrene ionomers for high performance anion exchange membrane water electrolysers, Nature Energy, 5 (2020) 378-385.

Chapter 4. Direct coated iridium nickel oxide on porous-transport layer as anode for high-performance proton-exchange membrane water electrolyzers

4.1. Introduction

Green hydrogen, which does not emit carbon dioxide, is attracting attention as a promising energy source. It is produced as the water electrolyzer that splits water into hydrogen and oxygen using electricity. Three types of water electrolyzer have been developed: Alkaline water electrolyzer (AWE), anion-exchange membrane water electrolyzer (AEMWE), and proton-exchange membrane water electrolyzer (PEMWE).[1, 2] Three water electrolyzers are classified by the type of electrolyte. AWE, AEMWE, and PEMWE are the water electrolyzer with the liquid alkaline electrolyte, anion-exchange membrane, and proton-exchange membrane (PEM), respectively. Among them, PEMWE showed the highest efficiency and stability because the PEM exhibited the highest ionic conductivity and stability.[3, 4] Additionally, the hydrogen purity is high due to the absence of liquid at the cathode where the hydrogen is produced. Despite these advantages, the high cost of PEMWE is considered as an obstacle to its commercialization.[5]

High-active oxygen evolution reaction (OER) catalysts have been widely proposed to improve the PEMWE performance. It is well known that Ir is the best OER catalyst in an acid electrolyte. To increase the OER activity and reduce the Ir loading, the introduction of transition metals on Ir as a form of alloy has been investigated.[6, 7] For example, various Ir-transition metal catalysts such as IrCu,[8, 9] IrCo,[10, 11] and IrNi[12, 13] showing superior activity and stability compared to the Ir have been developed. Zhou et al.[9] developed IrCu alloy OER catalyst showing high OER activity at 10 mA cm^{-2} of 270-290 mV. The high OER activity

is attributed to the modified electronic structure in Ir. Ma et al. [10] synthesized the IrCo@$IrCoO_x$ nanoparticles as the OER catalyst. The catalysts exhibited higher activity (260-385 mV at 10 mA cm^{-2}) compared to the Ir/C (452 mV at 10 mA cm^{-2}), showing its high stability. They stated that the high OER activity could be owing to the promoted water adsorption.[10] Reier et al.[12] proposed IrNi oxide OER catalyst, exhibiting 20 times activity enhancement. They mentioned that the high OER activity of IrNi is due to the low binding energy caused by the coverage of surface hydroxyls. Among the developed OER catalysts, IrNi-based catalysts exhibited the highest OER activity and stability with low binding energy of oxygen intermediates compared to the Ir-based catalyst.[14]

The electrode designs with ultra-low catalyst loading have been developed to enhance the PEMWE performance with low-cost. In the conventional electrode, the catalyst nanoparticles were stacked in a form of layer with the thickness of a few micrometers. Also, to prepare the dense layer consisting of catalyst nanoparticles, the polymeric ionomer was introduced as the binder and ion conductor. However, the thick catalyst layer and the use of non-conductive ionomer led to the increase in ohmic resistance. To address these disadvantages, the alternative electrode designs have been developed: macroporous electrode,[15] wire-stacked electrode,[16] and directly coated electrode.[17, 18] Because these designs are three-dimensional porous electrode without the polymeric ionomer, they can reduce the ohmic resistance, and thereby increasing PEMWE performance.[19]

Here we develop a directly coated anode with $IrNiO_x$ (directly coated $IrNiO_x$ electrode) to enhance the PEMWE performance. Figure 4.3.1(a) illustrates the PEMWEs with the $IrNiO_x$ electrode and the sprayed electrode using the commercial IrO_2 nanoparticles. While the commercial IrO_2 nanoparticles were densely packed with non-conductive ionomer in the sprayed IrO_2 anode, the $IrNiO_x$ thin film was directly deposited onto the PTL in the directly coated $IrNiO_x$ anode. The directly coated $IrNiO_x$ electrode can enhance the OER activity, electron

transport, and mass transport due to its electrode structure. To attain the high-active $IrNiO_x$ electrode, the electrodes with different ratio of Ir to Ni were developed using co-electrodeposition. As a result of the investigation, the $IrNiO_x$ electrodeposited using 7: 3 precursor solution (7_3) showed the highest OER activity and PEMWE performance among the five $IrNiO_x$ electrodes. Also, various membrane-electrode assembly (MEA) parameters, i.e. catalyst compositions, porous-transport layer (PTL) types, and hot-pressing process, were investigated to determine the PEMWE with the directly coated electrode. As a result, the performance of PEMWE with the optimized 7_3 electrode was higher than that with the commercial IrO_2 electrode, showing the highest performance reported to date.

4.2. Experimental

Preparation of $IrNiO_x$ electrodes and conventional electrode

The $IrNiO_x$ electrodes with different ratios of Ir to Ni were prepared using co-electrodeposition. Five electrodes were electrodeposited on the carbon paper (C-PTL; JNTG40, JNTG, Republic of Korea) or titanium paper (Ti-PTL; CNL Co., Republic of Korea) using different precursor solutions. Iridium (III) chloride hydrate ($IrCl_3 \cdot xH_2O$; Sigma Aldrich Co., USA) and Nickel (II) chloride hexahydrate ($NiCl_2 \cdot 6H_2O$; Sigma Aldrich Co., USA) were chosen as the Ir and Ni precursor, respectively. Using these precursors, the solution was prepared using the modified method reported in the literature. [17] (10-x) mM $IrCl_3 \cdot xH_2O$, x mM $NiCl_2 \cdot 6H_2O$, 100 mM hydrogen peroxide, 40 mM oxalic acid, 340 mM potassium carbonate, and distilled water (DI water) was used in the solution (x: 0, 3, 5, 7, and 10). The $IrNiO_x$ electrodes with different x of 0, 3, 5, 7, and 10 were referred as the 10_0, 7_3, 5_5, 3_7, and 0_10). The co-electrodeposition was conducted based on a three-electrode cell using C-PTL or Ti-PTL as the working electrode. Platinum mesh (Alfa aesar Co., USA) and Ag/AgCl electrode (SCE; CH instruments Co., USA) were employed as the counter and reference electrode, respectively. A constant voltage of 0.7 V vs. SCE was conducted for 10 min to fabricate five $IrNiO_x$ electrodes. After the co-electrodeposition, the prepared electrodes were washed using DI water to remove the residues. The conventional electrode was also prepared as the comparison sample to $IrNiO_x$ electrode. It was fabricated using spraying method reported in previous study. The spray slurry included commercial IrO_2 catalyst (Alfa aesar Co., USA), Nafion^{TM} ionomer (Dupont Co., Germany), DI water, and isopropanol (Sigma Aldrich Co., USA). The catalyst loading and ionomer content was 2.0 mg cm^{-2} and 10 wt. %.

Physicochemical characterization

The surface morphologies of the $IrNiO_x$ electrodes were investigated using Field-emission scanning electron microscopy (FE-SEM; SUPRA 55VP, Carl Zeiss, Germany). The cross-section morphology of $IrNiO_x$ electrodes was examined using FE-SEM (AURIGA, Carl Zeiss, Germany) and Focused ion beam (FIB; AURIGA, Carl Zeiss, Germany). EDX analysis was used to investigate the elemental mapping of $IrNiO_x$ electrodes. X-ray photoelectron spectroscopy (XPS; AXIS SUPRA, Kratos, U.K) was employed to analyze the chemical states of electrodes. The chemical compositions were examined using X-ray diffraction (XRD; JP/D/MAX-2500H, Regaku, USA). The IrNi loadings and ratios of Ir to Ni in the $IrNiO_x$ electrode were measured using an inductively coupled plasma-mass spectrometer (ICP-MS; Varian 820-MS, Varian, Australia).

Electrochemical characterization

The OER catalytic activities of the directly coated $IrNiO_x$ electrodes were evaluated in 0.1 M $HClO_4$ electrolyte. The active area was 1 cm^2. The sprayed IrO_2 electrode was employed as the reference electrode. In the sprayed electrode, a commercial IrO_2 nanoparticles (Alfa Aesar Co., USA) with the Nafion ionomer (Dupont Co., Germany) of 10 wt.% and the catalyst loading of 1.0 mg cm^{-2} were fabricated. The three-electrode cell was employed using five $IrNiO_x$ electrode and sprayed electrode, platinum mesh and Ag/AgCl electrode as the working, counter and reference electrodes, respectively. Linear sweep voltammetry (LSV) was performed using a potentiostat (Metrohm Autolab Co., Netherlands). The voltage was conducted from 1.25 to 1.65 V vs. reversible hydrogen electrode (RHE). The scan rate was 10 mV s^{-1}. The chronopotentiomery was applied at a constant current density of 10 mA cm^{-2} for 50 h to investigate the stability of the $IrNiO_x$ electrode.

PEMWE single-cell test

The PEMWE performance was evaluated based on a single-cell test with an active area of 5 cm^2. The Nafion212™ (Dupont Co., Germany) with the thickness of 50 μm was used as a PEM. The prepared $IrNiO_x$ electrode and conventional electrode were applied in the anode. In the cathode, Pt/C catalyst was sprayed onto the PEM with a loading of 0.4 mg cm^{-2} and Nafion ionomer content of 30 wt.%. Carbon paper (JNTG40-A3, JNTG Co, Republic of Korea) was used in the cathode PTL. The anode, cathode, and PEM were assembled with or without the hot-pressing process to fabricate the PEMWE single-cell. The hot-pressing condition is the temperature of 130 °C and the pressing time of 10 min. The cell temperature was maintained at 80 °C using a heating system. The DI water was chosen as the reactant of PEMWE. After pre-heated at 60 °C, it was supplied into the anode. The flow rate of reactant was 1 ml min^{-1}. Polarization curve was measured to evaluate the effect of the prepared electrode on practical PEMWE performance. The voltage was applied on the anode with a scan from 1.25 to 2.05 V The scan rate was 10 mV s^{-1}. Cyclic voltammetry (CV) was applied to compare the electrochemical surface area (ECSA). The directly coated and the sprayed electrode were used in the working electrode. The 40 wt.% Pt/C with the loading of 0.2 mg cm^{-2} was employed as the counter electrode. The fully humified hydrogen (150 mL min^{-1}) and nitrogen (200 mL min^{-1}) were supplied into the counter and working electrode, respectively. The scan rates with 10, 50, 100, 150, and 200 mV s^{-1} were applied.

4.3. Results and discussion

Preparation and physical characterizations of $IrNiO_x$ electrodes

The directly coated $IrNiO_x$ electrodes were synthesized using the co-electrodeposition where various kinds of precursors were applied simultaneously. To deposit the $IrNiO_x$ electrode, $IrCl_3 \cdot xH_2O$ and $NiCl_2 \cdot 6H_2O$ were employed as the Ir and Ni precursor, respectively. By adjusting the ratios of Ir to Ni precursor in the ED solution, five $IrNiO_x$ electrodes consisting of different ratios of Ir to Ni were synthesized. Five $IrNiO_x$ electrodes (10_0, 7_3, 5_5, 3_7, and 0_10) were electrodeposited onto the PTL using different precursor solutions with the ratio of Ir to Ni of 10: 0, 7: 3, 5: 5, 3: 7, and 0: 10. These electrodes were fabricated using anodic electrodeposition with the applied voltage of 0.7 V vs. SCE.[17]

Top-view morphologies of five $IrNiO_x$ electrodes and pristine PTL were presented in Figure 4.3.1(b) and Figure 4.3.2. As shown in FE-SEM images, the pristine PTL consists of the polytetrafluoroethylene (PTFE) coating between the carbon framework. For the five electrodes, $IrNiO_x$ layers with the form of thin film were deposited onto and between the carbon framework. Figure 1c shows the cross-view FE-SEM image after the FIB analysis of the 7_3 electrode. Especially, the $IrNiO_x$ layer with the thickness of approximately 100 – 200 nm was synthesized onto the framework of carbon PTL (Figure 4.3.1(c)). Also, the EDX images (Figure 4.3.1(d-g)) show that the Ir, Ni, and O atoms uniformly distributed in the $IrNiO_x$ layer on the carbon PTL. These results indicate that the $IrNiO_x$ thin film was well-developed on the directly coated electrode.

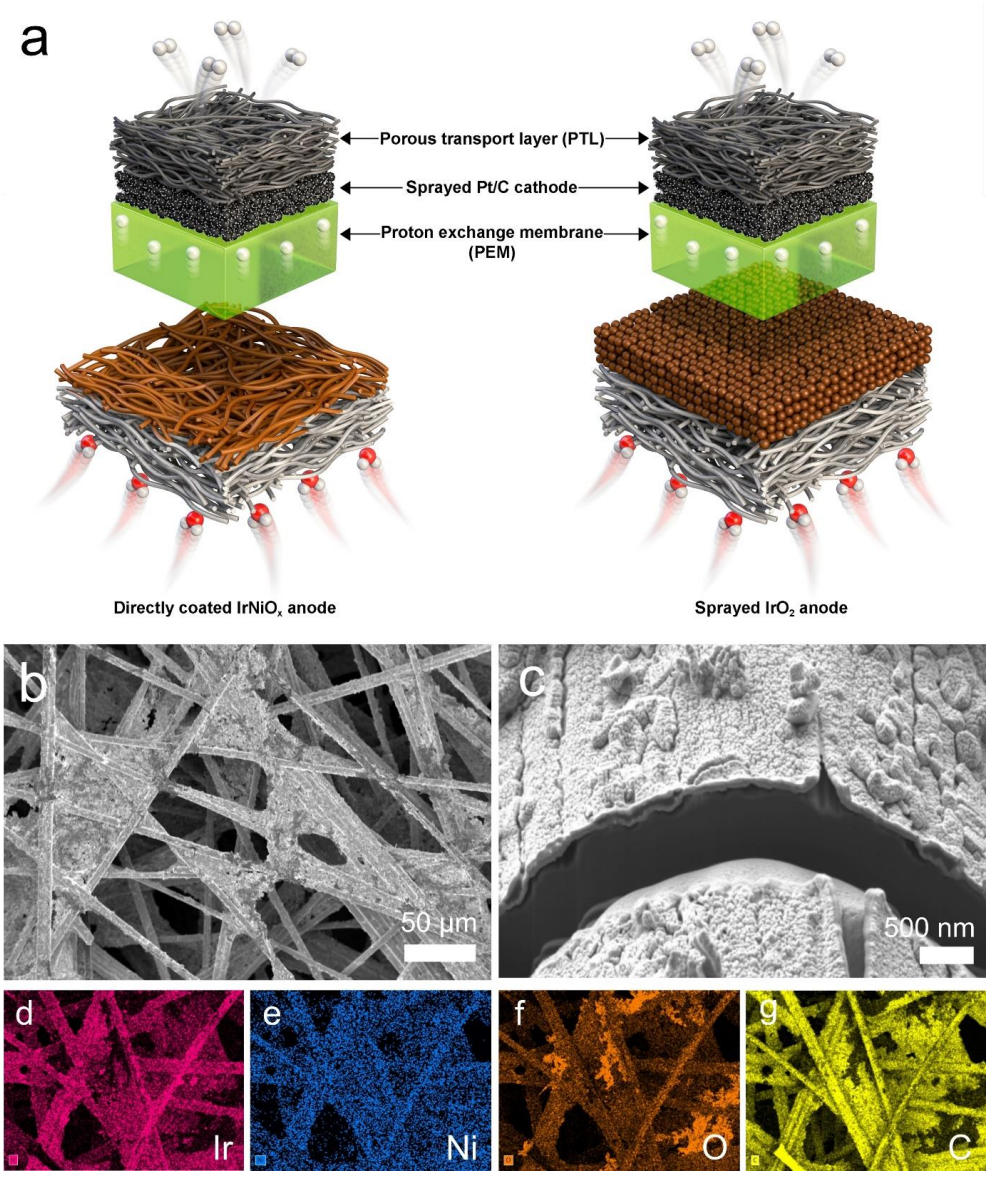

Figure 4.3.1 (a) Schematic diagrams of PEMWEs with the directly coated $IrNiO_x$ electrode and the sprayed IrO_2 electrode. (b) Top-view and (c) cross-section view after FIB analysis of FE-SEM image of $IrNiO_x$ electrode. (d-g) Elemental mapping of EDX analysis of $IrNiO_x$ electrode.

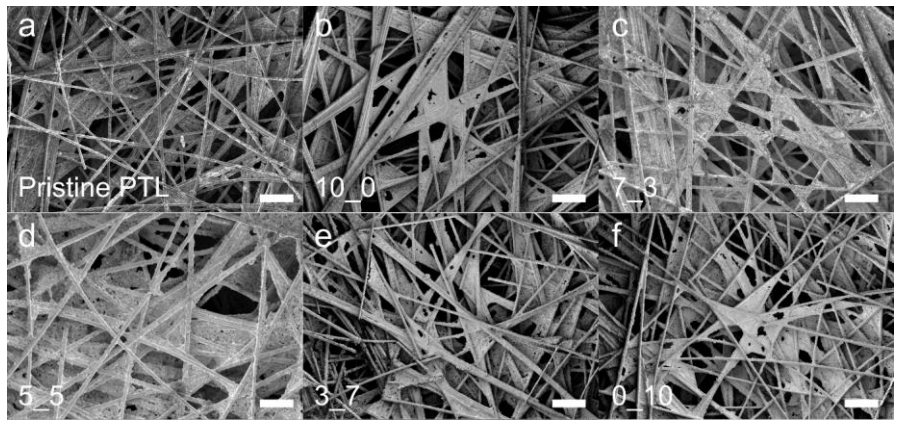

Figure 4.3.2 Field-emission scanning electron microscopy images of (a) pristine porous transport layer (PTL), (b–f) $IrNiO_x$ electrodes: (b) 10_0, (c) 7_3, (d) 5_5, (e) 3_7, and (f) 0_10. The scale bar is 100 μm.

Chemical characterizations of $IrNiO_x$ electrodes

The chemical compositions of $IrNiO_x$ electrodes were presented in Figure 4.3.3. Figure 4.3.3(a-b) present the Ir 4f and Ni 2p XPS spectra of $IrNiO_x$ electrodes. The Ir 4f of 10_0 shows binding energies of 61.9 for Ir $4f_{7/2}$ and 65.0 for Ir $4f_{5/2}$, with two shakeup satellites, which are associated with Ir^{4+} and Ir^{3+}. [20] With respect to $IrNiO_x$, additional peaks near 67.0 and 68.1 eV correspond to a spin-orbit doublet and shakeup satellite of Ni 3p.[21] The binding energies of Ir $4f_{7/2}$ and Ir $4f_{5/2}$ was shifted to the high binding energies of ~ 62.2 and ~ 65.2 eV, as the contents of Ni precursor increased in the ED solution. The XPS spectra peaks for 7_3 located at 843.1 and 855.6 eV are referred to Ni $2p_{3/2}$ and Ni $2p_{1/2}$ with two shakeup satellites.[21] The corresponding binding energies for Ni $2p_{3/2}$ and Ni $2p_{1/2}$ of 0_10 was also shifted to ~ 854.9 and ~ 872.1 eV as the contents of Ni precursor increased.[12] The positive shift in Ir 4f and Ni 2p doublet positions with an increase in Ni content indicates the modification of the electronic structure of $IrNiO_x$ for the different compositions. [12, 21]

Figure 4.3.3(c) shows the XRD spectra of $IrNiO_x$ electrodes. Peaks indexed to C substrate (JCPDS 41-1487) exist in the XRD spectra.[22, 23] The characteristic peak at approximately 26º was seen in all $IrNiO_x$ electrodes. By contrast, no peaks corresponding to Ir and Ni were observed in Figure 4.3.3(c). This XRD result suggests that the directly coated $IrNiO_x$ electrodes exhibit an amorphous phase. It is reported that amorphous phase existed in the electrodes prepared using electrodeposition process.[24, 25] Also, the ratios of Ir to Ni in $IrNiO_x$ electrodes were analyzed using the ICP-MS, shown in Figure 2d. The Ir: Ni ratios of the 10_0, 7_3, 5_5, 3_7, and 0_10 electrodes were approximately 10: 0, 5: 5, 3: 7, 1: 9, and 0: 10, respectively. According the results, the 10_0, 7_3, 5_5, 3_7, and 0_10 electrodes were named as IrO_x, $Ir_{0.5}Ni_{0.5}O_x$, $Ir_{0.3}Ni_{0.7}O_x$, $Ir_{0.1}Ni_{0.9}O_x$, and NiO_x. Also, the IrNi loadings in the 10_0, 7_3, 5_5, 3_7, and 0_10 electrodes were 0.52, 0.50, 0.82, 0.65, and 0.86 mg cm^{-2}, respectively.

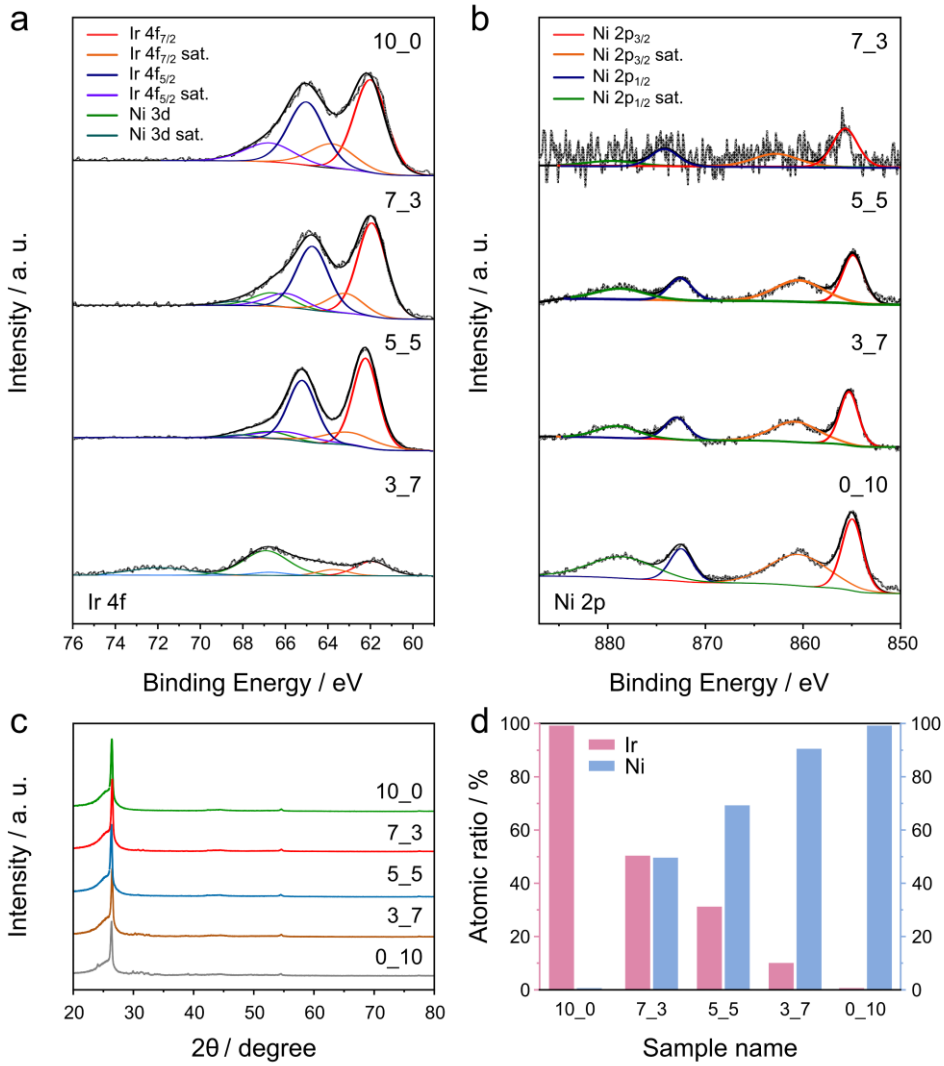

Figure 4.3.3 (a) Ir 4f and (b) Ni 2p of XPS spectra, (c) XRD spectra, and (d) the compositions of Ir and Ni measured by ICP-MS of five $IrNiO_x$ electrodes (10_0, 7_3, 5_5, 3_7, and 0_10).

Electrochemical characterizations of $IrNiO_x$ electrodes

The OER catalytic activities of the directly coated IrO_x $IrNiO_x$ ($Ir_{0.5}Ni_{0.5}O_x$, $Ir_{0.3}Ni_{0.7}O_x$, and $Ir_{0.1}Ni_{0.9}O_x$), and NiO_x electrodes were explored using half-cell tests. Figure 3a presents the LSV curves of five electrodes in a 0.1 M $HClO_4$. The NiO_x electrode showed significant low OER catalytic activity. When the amount of Ir, the catalyst that catalyzed by OER, was increased, the OER activity was enhanced. Among the $IrNiO_x$ electrodes, the $Ir_{0.5}Ni_{0.5}O_x$ exhibited the highest activity due to high Ir amount. Furthermore, the $Ir_{0.5}Ni_{0.5}O_x$ electrode (350 mV at 10 mA cm^{-2}) exhibited higher catalytic activity compared to the IrO_x electrode (385 mV at 10 mA cm^{-2}). This indicates that the addition of Ni in the IrO_x electrode enhanced the catalytic activity, which is consistent with the results reported to date.[12, 13] Figure 3b shows the Tafel plots of five electrodes. The Tafel slopes of the IrO_x, $Ir_{0.5}Ni_{0.5}O_x$, $Ir_{0.3}Ni_{0.7}O_x$, and $Ir_{0.1}Ni_{0.9}O_x$ and NiO_x electrode were 127.08, 126.44, 127.65, 230.88, and 302.35 mV dec^{-1}, respectively. The $Ir_{0.5}Ni_{0.5}O_x$ was the lowest among the samples. These results indicate that the $Ir_{0.5}Ni_{0.5}O_x$ electrode synthesized using precursor with the ratio of Ir to Ni of 7: 3 has the highest OER activity in acid electrolyte. The catalytic stability of the $Ir_{0.5}Ni_{0.5}O_x$ electrode was shown in the Figure 4.3.4(c). The OER stability of the $Ir_{0.5}Ni_{0.5}O_x$ electrode was evaluated under a constant current density of 10 mA cm^{-2} for 50 h. The overpotential at 10 mA cm^{-2} of the $Ir_{0.5}Ni_{0.5}O_x$ electrode was maintained without a significant increase. Therefore, the $Ir_{0.5}Ni_{0.5}O_x$ is determined to be a suitable OER catalyst in the anode of PEMWE exhibiting the high-active and stable activity, among the prepared directly coated electrodes.

The OER catalytic activities of the directly coated $Ir_{0.5}Ni_{0.5}O_x$, electrode and commercial IrO_2 were compared, as shown in Figure 4.3.5(a). The directly coated $Ir_{0.5}Ni_{0.5}O_x$ electrode exhibited slightly higher than the commercial IrO_2 nanoparticle (commercial_IrO_2). Also, the Tafel plot of the $Ir_{0.5}Ni_{0.5}O_x$ electrode was slightly lower than that of commercial IrO_2 (128.08 mV dec^{-1}) (Figure

4.3.5(b)). Also, the comparison of the catalytic stabilities of the $Ir_{0.5}Ni_{0.5}O_x$ electrode was shown in the Figure 4.3.5(c). The OER stabilities of the electrodes were performed under a constant current density of 10 mA cm^{-2} for 50 h. The overpotential at 10 mA cm^{-2} of the commercial_IrO_2 electrode was gradually increased for 50 h, which could be owing to the detachment of catalyst nanoparticles. By contrast, the $Ir_{0.5}Ni_{0.5}O_x$ electrode showed the maintained overpotential without a significant increase. Therefore, the $Ir_{0.5}Ni_{0.5}O_x$ exhibited slightly higher OER activity and better durability in an acidic electrode compared to the commercial IrO_2 nanoparticles.

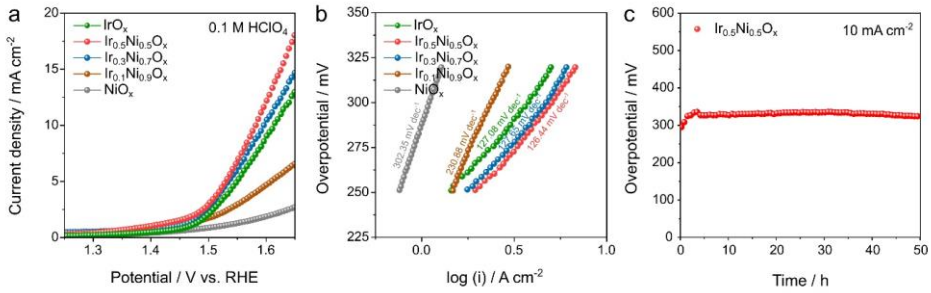

Figure 4.3.4 (a) Linear sweep voltammograms of five $IrNiO_x$ electrodes (IrO_x, $Ir_{0.5}Ni_{0.5}O_x$, $Ir_{0.3}Ni_{0.7}O_x$, $Ir_{0.1}Ni_{0.9}O_x$, and NiO_x) in 0.1 M $HClO_4$ solution. (b) Tafel plots of IrO_x, $Ir_{0.5}Ni_{0.5}O_x$, $Ir_{0.3}Ni_{0.7}O_x$, $Ir_{0.1}Ni_{0.9}O_x$, and NiO_x electrodes derived from Figure 4.3.4(a). (c) Stability test of $Ir_{0.5}Ni_{0.5}O_x$ electrode conducted at a constant current density of 10 mA cm^{-2} for 50 h.

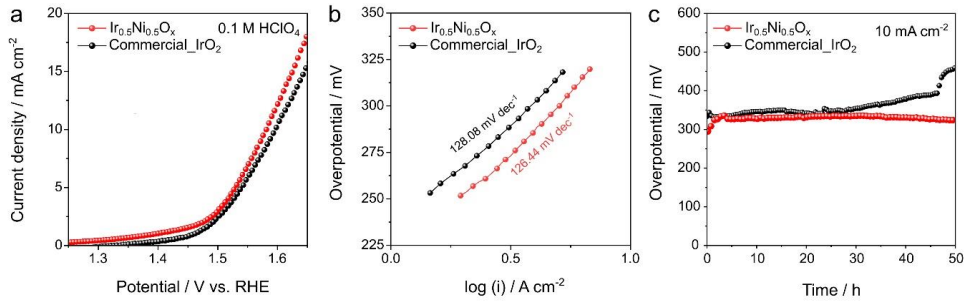

Figure 4.3.5 (a) Linear sweep voltammograms of the directly coated $Ir_{0.5}Ni_{0.5}O_x$ and the sprayed IrO_2 electrodes in 0.1 M $HClO_4$ solution. (b) Tafel plots of the directly coated $Ir_{0.5}Ni_{0.5}O_x$ and the sprayed IrO_2 electrodes derived from Figure S2(a). (c) A comparison of the stability tests of the directly coated $Ir_{0.5}Ni_{0.5}O_x$ and the sprayed IrO_2 electrodes conducted at a constant current density of 10 mA cm^{-2} for 50 h.

Effect of MEA parameters for PEMWE with $IrNiO_x$ electrodes.

Various MEA parameters, such as the effect of the catalyst compositions, the PTL types, and the presence/absence of hot-pressing process were investigated to achieve high-performance PEMWE with the directly coated $IrNiO_x$ electrodes. To investigate the effect of ratio of Ir to Ni in the $IrNiO_x$ electrode on the PEMWE performance, the PEMWEs with different $IrNiO_x$ electrodes were prepared and evaluated. Figure 4.3.6(a) presents the single-cell performance of PEMWEs with the IrO_x, $Ir_{0.5}Ni_{0.5}O_x$, $Ir_{0.3}Ni_{0.7}O_x$, $Ir_{0.1}Ni_{0.9}O_x$, and NiO_x electrodes (IrO_x, $Ir_{0.5}Ni_{0.5}O_x$, $Ir_{0.3}Ni_{0.7}O_x$, $Ir_{0.1}Ni_{0.9}O_x$, and NiO_x). The performance at 1.6 V was increased in the order of $Ir_{0.5}Ni_{0.5}O_x$ > $Ir_{0.3}Ni_{0.7}O_x$ > IrO_x > $Ir_{0.1}Ni_{0.9}O_x$ >NiO_x. The trend is consistent with the results of the OER activities obtained using the half-cell test (Figure 4.3.4(a-b)). In addition to the half-cell test, the single-cell test showed that the $Ir_{0.5}Ni_{0.5}O_x$ exhibited the highest PEMWE performance among the electrodes. The effect of PTL types on the PEMWE performance was presented in Figure 4.3.6(b). Carbon[17, 26] and titanium paper [18, 26, 27] have been widely applied as the anode PTL for PEMWE. To compare the performance of PEMWE with different PTLs, two anode PTL types were employed as the substrate of the directly coated IrO_x electrode to prepare two PEMWEs (IrO_x_C and IrO_x_Ti). The performance at 1.6 V of the IrO_x_Ti was higher than that of the IrO_x_C. This difference is ascribed to the effect of electrical conductivity of PTL. The titanium paper exhibited smaller sheet resistance than the carbon paper, indicating that it had higher electrical conductivity. In addition, the titanium paper can be more corrosion resistive compared to the carbon paper. The carbon corrosion can easily happen under high voltage in acidic electrolyte. Thus, the titanium paper is optimal PTL for the directly coated electrode for PEMWE.

The effect of hot-pressing process was examined to enhance the PEMWE performance using the directly coated electrode. As mentioned above, the PEMWE with the directly coated electrode exhibited still low performance at 1.6 V of ~ 100

mA cm^{-2}. To increase the PEMWE performance, an additional hot-pressing process is applied. Figure 4.3.6(c) shows the polarization curves of PEMWEs with the IrO_x electrodes with and without the hot-pressing process. When the MEA was prepared without the hot-pressing process, the PEMWE performance was significantly low, showing the current density at 1.6 V of 56 mA cm^{-2}. On the other hand, the application of hot-pressing process in the MEA fabrication resulted in a sharp performance enhancement. This implies that the hot-pressing is necessary process for the fabrication of the MEA incorporated with the directly coated electrode. For the conventional electrode fabricated using the spraying method, the direct spraying of the catalyst slurry onto the membrane can enhance the membrane/electrode interface. On the other hand, the interface between membrane and the directly coated electrode is difficult as they are separate. The hot-pressing could improve their interface, which is attributed to the enhanced adhesion.[28, 29] Therefore, the additional hot-pressing process is required to prepare PEMWE with the directly coated electrode.

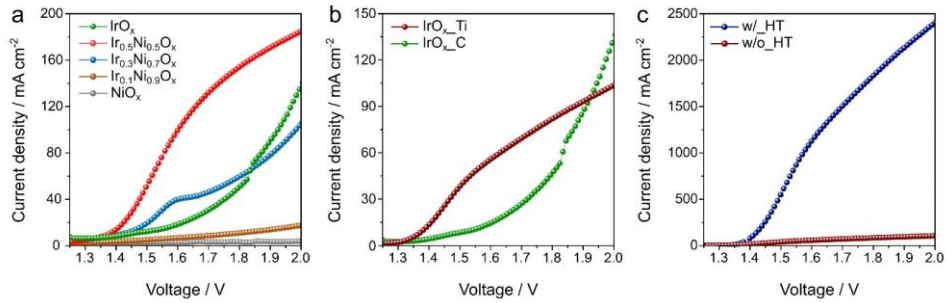

Figure 4.3.6 (a) Polarization curves of PEMWEs incorporating five $IrNiO_x$ electrodes (IrO_x, $Ir_{0.5}Ni_{0.5}O_x$, $Ir_{0.3}Ni_{0.7}O_x$, $Ir_{0.1}Ni_{0.9}O_x$, and NiO_x) coated on the carbon paper. (b) Performances of PEMWEs with the IrO_x electrodes with different substrates (Ti_paper and C_paper). (c) Polarization curves of PEMWEs using the IrO_x electrodes prepared with and without the hot-pressing process (w/_HT and w/o_HT). The cell temperature was maintained at 80 ºC. The preheated DI water was fed into the anode with a flow rate of 1 ml min^{-1}.

Single-cell performance of PEMWE with the optimized $Ir_{0.5}Ni_{0.5}O_x$ electrode and the sprayed IrO_2 electrode.

Figure 5a shows the polarization curves of the PEMWE with the optimized directly coated electrode (DC_$Ir_{0.5}Ni_{0.5}O_x$) and the sprayed IrO_2 electrode (Commercial_IrO_2). The current densities at 1.6 V of the DC_$Ir_{0.5}Ni_{0.5}O_x$) and the commercial_IrO_2 were 1350 and 925 mA cm^{-2}, respectively. Although the $Ir_{0.5}Ni_{0.5}O_x$ had a similar catalyst activity with the commercial IrO_2 nanoparticles (Figure 4.3.5(a)), the DC_$Ir_{0.5}Ni_{0.5}O_x$ showed much higher PEMWE performance than the commercial IrO_2. The PEMWE performance enhancement is due to two effects: the electrode design effect and the alloy effect. As shown in Figure 4.3.8(a), the PEMWEs with the directly coated IrO_x electrode (DC_IrO_x) and the sprayed electrode with commercial IrO_2 were evaluated to prove the electrode design effect. The performance enhancement in low current densities region was observed, which is the difference in electrode design. On the other hand, the performance of DC_ $Ir_{0.5}Ni_{0.5}O_x$ was enhanced in high current densities region compared to the DC_IrO_x electrode. This is owing to the introduction of Ni into the IrO_X. We can conclude that the high PEMWE performance of DC_ $Ir_{0.5}Ni_{0.5}O_x$ electrode was attributed to the synergistic effect of electrode design and alloy. The DC_$Ir_{0.5}Ni_{0.5}O_x$ exhibited 1.46 times higher performance at 1.6 V compared to the commercial_IrO_2. In addition, the achieved performance is the highest value among the research on anode of PEMWE despite its low catalyst loading.[15-18, 30-36]

The ECSAs of the DC_ $Ir_{0.5}Ni_{0.5}O_x$ and the commercial_IrO_2 were compared in Figure 4.3.7(c). The ECSA was estimated by measuring the double-layer capacitance obtained at various scan rates of CV curves in a non-faradaic region which is a range of 0.2 to 0.3 V_{RHE}.[37, 38] Figure 4.3.7(c) presents the curves of total currents for the PEMWEs with the DC_ $Ir_{0.5}Ni_{0.5}O_x$ and the commercial_IrO_2 at the corresponding scan rate. The slope of the DC_ $Ir_{0.5}Ni_{0.5}O_x$ was higher than that of the commercial_IrO_2 electrode, implying that the DC_$Ir_{0.5}Ni_{0.5}O_x$ had larger

ECSA. Due to its larger ECSA, the DC_$Ir_{0.5}Ni_{0.5}O_x$ electrode exhibited higher PEMWE performance than the commercial_IrO_2 electrode.

The pore-size distributions of two electrodes were analyzed in Figure 4.3.7(d). The pores in the electrodes were measured using the mercury porosimeter. The pores with size of 20 – 40 nm were mainly developed in the commercial_IrO_2 electrode. The developed pores are the secondary pores formed when the IrO_2 nanoparticles were deposited using the spraying method with the catalyst slurry. Unlike the commercial_IrO_2 electrode, the DC_ $Ir_{0.5}Ni_{0.5}O_x$ electrode had the larger pores with the size of 40 – 100 μm. It is the $Ir_{0.5}Ni_{0.5}O_x$ layer directly coated onto the PTL. The DC_ $Ir_{0.5}Ni_{0.5}O_x$ electrode had its porous structure similar with the that of PTL. These results indicate that the DC_ $Ir_{0.5}Ni_{0.5}O_x$ electrode had the larger pores compared to the commercial_IrO_2 electrode.

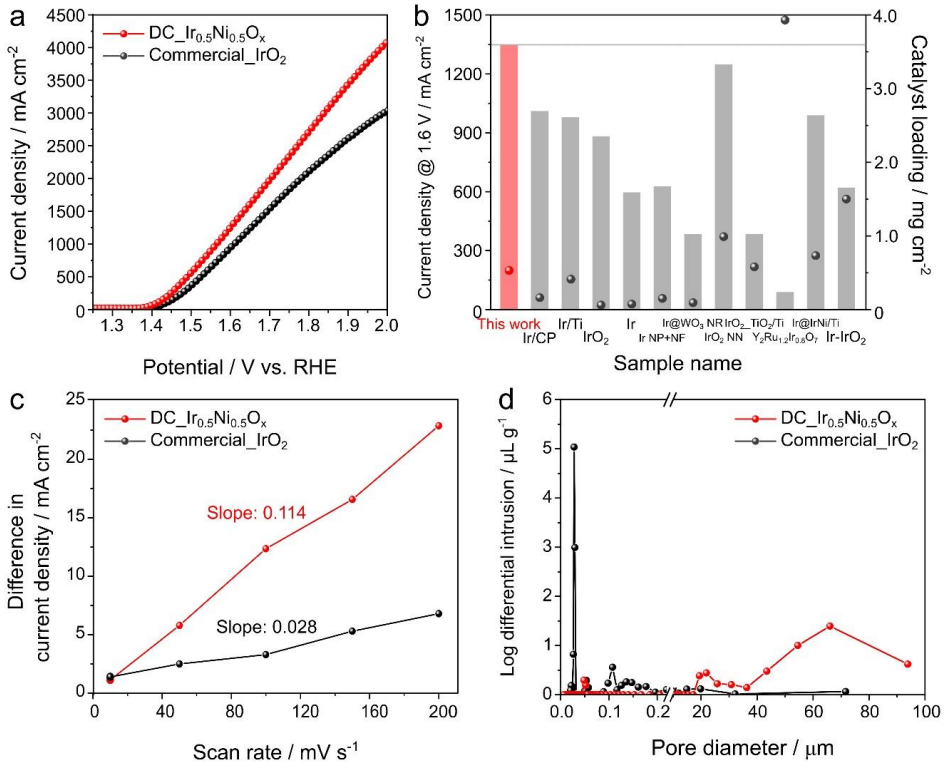

Figure 4.3.7 (a) Polarization curves of PEMWE using $Ir_{0.5}Ni_{0.5}O_x$ electrode ($DC\_Ir_{0.5}Ni_{0.5}O_x$) and commercial IrO_2 nanoparticles ($Commercial\_IrO_2$). The Ti paper was employed as the anode PTL. The hot-pressing was applied to prepare MEA. The catalyst loading was 0.5 mg cm^{-2}. The cell temperature was maintained at 80 ºC. The preheated DI water was fed into the anode with a flow rate of 1 ml min^{-1}. (b) Comparison of the performance achieved in this study with those reported in the literature. (c) Plot of current density differences of the $DC\_Ir_{0.5}Ni_{0.5}O_x$ and the $commercial\_IrO_2$ against scan rates from CV. (d) Pore-size distribution of $Ir_{0.5}Ni_{0.5}O_x$ electrode and commercial electrode.

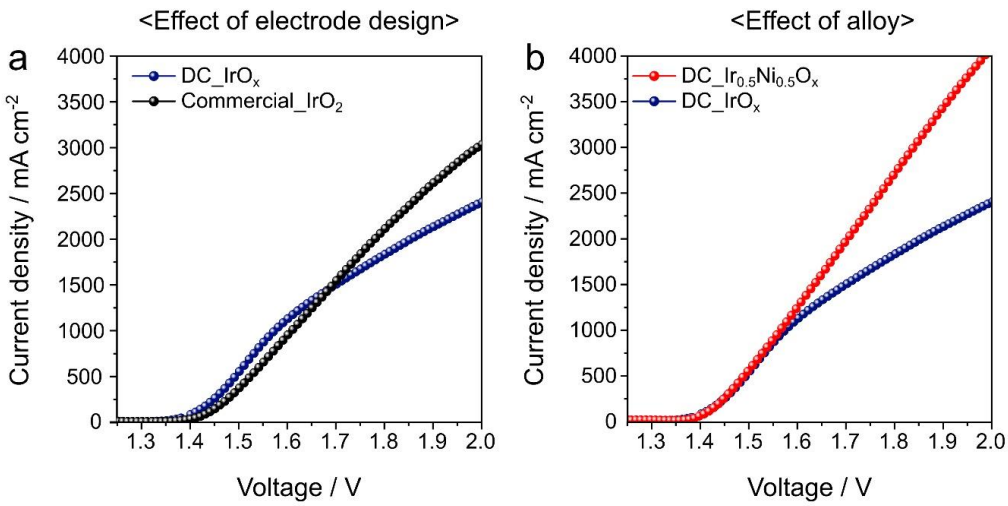

Figure 4.3.8 (a) Polarization curves of PEMWEs incorporated with the DC_IrO_x and the $commercial\_IrO_2$ electrodes. (b) Performances of PEMWEs with the $DC\_Ir_{0.5}Ni_{0.5}O_x$ and the DC_IrO_x electrodes. The cell temperature was maintained at 80 ºC. The preheated distilled (DI) water was supplied to the anode at a flow rate of 1 mL min^{-1}.

4.4. Conclusion

The development of high-performance anode design is important for low-cost proton-exchange membrane water electrolyzer (PEMWE). In this study, we report an iridium nickel oxide directly coated anode ($IrNiO_x$ electrode) for high-efficient PEMWE. Five $IrNiO_x$ electrodes with different ratio of Ir to Ni were developed using co-electrodeposition. The resulting electrodes consist of thin $IrNiO_x$ layer on the Ti substrate. To develop the PEMWE incorporating $IrNiO_x$ electrode, the effect of catalyst compositions, porous transport layer (PTL), and fabrication methods were investigated. As a result, the directly coated $Ir_{0.5}Ni_{0.5}O_x$ electrode (350 mV at 10 mA cm^{-2}) exhibited higher OER activity compared to the directly coated IrO_x electrode (385 mV at 10 mA cm^{-2}) and the sprayed IrO_2 electrode (mV at 10 mA cm^{-2}). Also, the performance of PEMWE with the $Ir_{0.5}Ni_{0.5}O_x$ electrode was higher than that with the IrO_x electrode. This is attributed to the increased electrochemical surface area due to the introduction of Ni in the Ir. As a result of the investigation of the MEA parameters, the PEMWE with optimized directly coated electrode was determined to fabricate the DC_$Ir_{0.5}Ni_{0.5}O_x$. When compared to the commercial_IrO_2, the electrode achieved outstanding PEMWE performance at 1.6 V of 1350 mA cm^{-2}, which is due to the synergistic effect of the IrNi alloy and the structural characteristics of the directly coated electrode.

4.5. References

[1] Q. Feng, X.Z. Yuan, G. Liu, B. Wei, Z. Zhang, H. Li, H. Wang, A review of proton exchange membrane water electrolysis on degradation mechanisms and mitigation strategies, Journal of Power Sources, 366 (2017) 33-55.

[2] H.A. Miller, K. Bouzek, J. Hnat, S. Loos, C.I. Bernäcker, T. Weißgärber, L. Röntzsch, J. Meier-Haack, Green hydrogen from anion exchange membrane water electrolysis: a review of recent developments in critical materials and operating conditions, Sustainable Energy & Fuels, 4 (2020) 2114-2133.

[3] M. Carmo, D.L. Fritz, J. Mergel, D. Stolten, A comprehensive review on PEM water electrolysis, International Journal of Hydrogen Energy, 38 (2013) 4901-4934.

[4] S. Shiva Kumar, V. Himabindu, Hydrogen production by PEM water electrolysis – A review, Materials Science for Energy Technologies, 2 (2019) 442-454.

[5] S. Stiber, N. Sata, T. Morawietz, S.A. Ansar, T. Jahnke, J.K. Lee, A. Bazylak, A. Fallisch, A.S. Gago, K.A. Friedrich, A high-performance, durable and low-cost proton exchange membrane electrolyser with stainless steel components, Energy & Environmental Science, 15 (2022) 109-122.

[6] Z. Chen, X. Duan, W. Wei, S. Wang, B.-J. Ni, Electrocatalysts for acidic oxygen evolution reaction: Achievements and perspectives, Nano Energy, 78 (2020) 105392.

[7] H. Wu, Y. Wang, Z. Shi, X. Wang, J. Yang, M. Xiao, J. Ge, W. Xing, C. Liu, Recent developments of iridium-based catalysts for the oxygen evolution reaction in acidic water electrolysis, Journal of Materials Chemistry A, 10 (2022) 13170-13189.

[8] W. Sun, Y. Song, X.-Q. Gong, L.-m. Cao, J. Yang, An efficiently tuned d-orbital occupation of IrO2 by doping with Cu for enhancing the oxygen evolution reaction activity, Chemical Science, 6 (2015) 4993-4999.

[9] L. Zhou, X. Liu, K. Wang, X. Zhao, H. Pu, T. Zhang, J. Jia, K. Dong, Y. Deng, One-Pot Synthesis of Alloy Ir–Cu Microspheres with Excellent Electro-Catalytic Activity Toward Oxygen Evolution Reaction under Acidic Conditions, Energy & Fuels, 34 (2020) 9956-9962.

[10] X. Ma, L. Deng, M. Lu, Y. He, S. Zou, Y. Xin, Heterostructure of core–shell IrCo@IrCoOx as efficient and stable catalysts for oxygen evolution reaction, Nanotechnology, 33 (2022) 125702.

[11] F. Mao, X. Zhao, Y. Chang, J. Jia, Controllable Construction of IrCo Nanoclusters and the Performance for Water Electrolysis, Catalysts, 12 (2022) 914.

[12] T. Reier, Z. Pawolek, S. Cherevko, M. Bruns, T. Jones, D. Teschner, S. Selve, A. Bergmann, H.N. Nong, R. Schlögl, K.J.J. Mayrhofer, P. Strasser, Molecular Insight in Structure and Activity of Highly Efficient, Low-Ir Ir–Ni Oxide Catalysts for Electrochemical Water Splitting (OER), Journal of the American Chemical Society, 137 (2015) 13031-13040.

[13] H.N. Nong, T. Reier, H.-S. Oh, M. Gliech, P. Paciok, T.H.T. Vu, D. Teschner, M. Heggen, V. Petkov, R. Schlögl, T. Jones, P. Strasser, A unique oxygen ligand environment facilitates water oxidation in hole-doped IrNiOx core–shell electrocatalysts, Nature Catalysis, 1 (2018) 841-851.

[14] Y. Wang, L. Zhang, K. Yin, J. Zhang, H. Gao, N. Liu, Z. Peng, Z. Zhang, Nanoporous Iridium-Based Alloy Nanowires as Highly Efficient Electrocatalysts Toward Acidic Oxygen Evolution Reaction, ACS Applied Materials & Interfaces, 11 (2019) 39728-39736.

[15] J.E. Park, S. Kim, O.-H. Kim, C.-Y. Ahn, M.-J. Kim, S.Y. Kang, T.I. Jeon, J.-G. Shim, D.W. Lee, J.H. Lee, Y.-H. Cho, Y.-E. Sung, Ultra-low loading of IrO2 with

an inverse-opal structure in a polymer-exchange membrane water electrolysis, Nano Energy, 58 (2019) 158-166.

[16] Y.J. Kim, A. Lim, J.M. Kim, D. Lim, K.H. Chae, E.N. Cho, H.J. Han, K.U. Jeon, M. Kim, G.H. Lee, G.R. Lee, H.S. Ahn, H.S. Park, H. Kim, J.Y. Kim, Y.S. Jung, Highly efficient oxygen evolution reaction via facile bubble transport realized by three-dimensionally stack-printed catalysts, Nature Communications, 11 (2020) 4921.

[17] B.-S. Lee, S.H. Ahn, H.-Y. Park, I. Choi, S.J. Yoo, H.-J. Kim, D. Henkensmeier, J.Y. Kim, S. Park, S.W. Nam, K.-Y. Lee, J.H. Jang, Development of electrodeposited IrO2 electrodes as anodes in polymer electrolyte membrane water electrolysis, Applied Catalysis B: Environmental, 179 (2015) 285-291.

[18] S. Choe, B.-S. Lee, M.K. Cho, H.-J. Kim, D. Henkensmeier, S.J. Yoo, J.Y. Kim, S.Y. Lee, H.S. Park, J.H. Jang, Electrodeposited IrO2/Ti electrodes as durable and cost-effective anodes in high-temperature polymer-membrane-electrolyte water electrolyzers, Applied Catalysis B: Environmental, 226 (2018) 289-294.

[19] M. Bernt, H.A. Gasteiger, Influence of Ionomer Content in IrO2/TiO2 Electrodes on PEM Water Electrolyzer Performance, Journal of The Electrochemical Society, 163 (2016) F3179.

[20] R.-S. Chen, Y.-S. Huang, Y.-M. Liang, D.-S. Tsai, Y. Chi, J.-J. Kai, Growth control and characterization of vertically aligned IrO2 nanorods, Journal of Materials Chemistry, 13 (2003) 2525-2529.

[21] Q. Wang, X. Huang, Z.L. Zhao, M. Wang, B. Xiang, J. Li, Z. Feng, H. Xu, M. Gu, Ultrahigh-Loading of Ir Single Atoms on NiO Matrix to Dramatically Enhance Oxygen Evolution Reaction, Journal of the American Chemical Society, 142 (2020) 7425-7433.

[22] Y. Zhang, C. Sun, H. Su, W. Huang, X. Dong, N-doped carbon coated hollow NixCo9−xS8 urchins for a high performance supercapacitor, Nanoscale, 7 (2015) 3155-3163.

[23] S.S. Mehta, D.Y. Nadargi, M.S. Tamboli, T. Alshahrani, V.R. Minnam Reddy, E.S. Kim, I.S. Mulla, C. Park, S.S. Suryavanshi, RGO/WO3 hierarchical architectures for improved H2S sensing and highly efficient solar-driving photo-degradation of RhB dye, Scientific Reports, 11 (2021) 5023.

[24] J. Kim, H. Kim, S.-K. Kim, S.H. Ahn, Electrodeposited amorphous Co–P–B ternary catalyst for hydrogen evolution reaction, Journal of Materials Chemistry A, 6 (2018) 6282-6288.

[25] C. Wang, Y. Wu, Z. Zhou, J. Wang, S. Pei, S. Liu, Electrodeposited amorphous nickel–iron phosphide and sulfide derived films for electrocatalytic oxygen evolution, International Journal of Hydrogen Energy, (2022).

[26] Z. Kang, S.M. Alia, J.L. Young, G. Bender, Effects of various parameters of different porous transport layers in proton exchange membrane water electrolysis, Electrochimica Acta, 354 (2020) 136641.

[27] H. Becker, E.J.F. Dickinson, X. Lu, U. Bexell, S. Proch, C. Moffatt, M. Stenström, G. Smith, G. Hinds, Assessing potential profiles in water electrolysers to minimise titanium use, Energy & Environmental Science, 15 (2022) 2508-2518.

[28] S. Martemianov, V.A. Raileanu Ilie, C. Coutanceau, Improvement of the proton exchange membrane fuel cell performances by optimization of the hot pressing process for membrane electrode assembly, Journal of Solid State Electrochemistry, 18 (2014) 1261-1269.

[29] M.K. Cho, H.-Y. Park, S. Choe, S.J. Yoo, J.Y. Kim, H.-J. Kim, D. Henkensmeier, S.Y. Lee, Y.-E. Sung, H.S. Park, J.H. Jang, Factors in electrode fabrication for performance enhancement of anion exchange membrane water electrolysis, Journal of Power Sources, 347 (2017) 283-290.

[30] F. Hegge, F. Lombeck, E. Cruz Ortiz, L. Bohn, M. von Holst, M. Kroschel, J. Hübner, M. Breitwieser, P. Strasser, S. Vierrath, Efficient and Stable Low Iridium Loaded Anodes for PEM Water Electrolysis Made Possible by Nanofiber Interlayers, ACS Applied Energy Materials, 3 (2020) 8276-8284.

[31] G. Jiang, H. Yu, Y. Li, D. Yao, J. Chi, S. Sun, Z. Shao, Low-Loading and Highly Stable Membrane Electrode Based on an Ir@WOxNR Ordered Array for PEM Water Electrolysis, ACS Applied Materials & Interfaces, 13 (2021) 15073-15082.

[32] T.L. Doan, H.E. Lee, M. Kim, W.C. Cho, H.S. Cho, T. Kim, Influence of IrO2/TiO2 coated titanium porous transport layer on the performance of PEM water electrolysis, Journal of Power Sources, 533 (2022) 231370.

[33] F. Gu, L. Zheng, H. Wei, W. Mi, C. Zhang, Q. Su, W. Zhu, W. Lin, Tuning amorphous Ir-IrOx oxygen evolution catalyst via precursor complexation for efficient and durable water electrolysis, Applied Surface Science, 606 (2022) 155008.

[34] J. Lim, G. Kang, J.W. Lee, S.S. Jeon, H. Jeon, P.W. Kang, H. Lee, Amorphous Ir atomic clusters anchored on crystalline IrO2 nanoneedles for proton exchange membrane water oxidation, Journal of Power Sources, 524 (2022) 231069.

[35] H. Liu, Z. Zhang, M. Li, Z. Wang, X. Zhang, T. Li, Y. Li, S. Tian, Y. Kuang, X. Sun, Iridium Doped Pyrochlore Ruthenates for Efficient and Durable Electrocatalytic Oxygen Evolution in Acidic Media, Small, 18 (2022) 2202513.

[36] K.-R. Yeo, K.-S. Lee, H. Kim, J. Lee, S.-K. Kim, A highly active and stable 3D dandelion spore-structured self-supporting Ir-based electrocatalyst for proton exchange membrane water electrolysis fabricated using structural reconstruction, Energy & Environmental Science, 15 (2022) 3449-3461.

[37] K. Fan, H. Chen, Y. Ji, H. Huang, P.M. Claesson, Q. Daniel, B. Philippe, H. Rensmo, F. Li, Y. Luo, L. Sun, Nickel–vanadium monolayer double hydroxide for efficient electrochemical water oxidation, Nature Communications, 7 (2016) 11981.

[38] S. Liu, Y. Jiang, M. Yang, M. Zhang, Q. Guo, W. Shen, R. He, M. Li, Highly conductive and metallic cobalt–nickel selenide nanorods supported on Ni foam as an efficient electrocatalyst for alkaline water splitting, Nanoscale, 11 (2019) 7959-7966.

국문 초록

수소는 이산화탄소 배출을 하지 않고, 높은 에너지 밀도를 나타내기 때문에 화석 연료를 대체할 수 있는 신재생 에너지원으로 각광받고 있다. 수소는 주로 증기 개질, 바이오매스 전환, 수전해를 통해 얻을 수 있다. 그 중에서도 수전해는 높은 에너지밀도를 가지고 있고, 탄소를 배출하지 않아 지속 가능한 수소 생산방법으로 주목받고 있다. 이와 관련하여 지금까지 전기촉매의 활성에 대한 연구는 광범위하게 진행되어 왔고, 상당한 진전을 이루었다. 그러나 반쪽전지에서의 우수한 활성은 단위전지에서의 성능으로 이어지지 않는데, 실제 수전해는 추가적인 실험적 요인을 고려해야 하기 때문이다.

알말리 수전해가 이미 상용화된 가운데, 양이온 교환 막 또는 음이온 교환 막을 포함하는 고분자 전해질 막을 이용한 고분자 전해질 막 수전해는 zero-gap 설계로 인한 높은 효율과 고순도의 수소 생산이 가능해 유망한 수전해 방법으로 간주된다.

본 논문에서, 여러가지 접근방법을 통해 고분자 전해질 막 수전해용 다공성 전극 구조를 단위 전지에서의 우수한 성능을 실현하였다.

제 1 장에서는, 뒤의 내용을 명확하게 이해하기 위해 양이온 교환 막 또는 음이온 교환 막을 이용한 수전해의 일반적인 개념을 설명한다.

제 2 장에서는, 아릴-에테르 골격 구조가 없는 음이온 교환 막을 이용한 고성능 및 안정적인 음이온 교환 막 수전해를 개발했다. 고성능 및 고내구성 음이온 교환 막 수전해의 개발을 위해 음이온 교환 막에 적합한 다양한 요소를 조사하였다. 그 결과 본 연구에서 채택한 음이온 교환 막은 기존보다 더 우수한 성능과 내구성을 보였다. 또한 순수한 물

공급 조건에서도 높은 효율을 나타냈다. 이러한 결과는 아릴-에테르 골격이 없는 고효율 및 고내구성 음이온 교환 막 때문이다.

제 3 장에서는, 음이온 교환 막 수전해의 3 차원 다공성 NiFe/Ni foam 전극이 개발되었다. 전극은 직류 및 펄스 전류를 인가하는 단순한 전착 공정으로 제작되었다. 비 전자전도성 고분자 물질을 사용하지 않은 이오노머 프리 전극은 기존의 입자 기반 전극보다 낮은 옴 저항으로 인해 더 높은 성능을 보였다. 3 차원 다공성 구조체는 비표면적을 효과적으로 향상시키고, 물질전달 저항을 감소시켰다. 이러한 조성 및 구조로 음이온 교환 막은 기존 입자기반 또는 비 다공성 전극에 비해 우수한 성능을 보였다.

제 4 장에서는, 고효율 양이온 교환 막 수전해를 위한 이리듐 니켈 산화물 직접 코팅 전극($IrNiO_x$ 전극)이 개발되었다. 동시 전착을 이용하여 Ir 과 Ni 의 비율이 다른 5 개의 $IrNiO_x$ 전극을 개발하였다. 개발된 전극은 탄소기판 위에 얇은 $IrNiO_x$ 층으로 이루어졌다. $IrNiO_x$ 전극을 이용한 양이온 교환 막 수전해를 개발하기 위해 제조방법, 촉매 조성물, 및 다공성 전달 층의 효과를 조사하였다. 그 결과, $IrNiO_x$ 는 7:3 전구체 용액으로 제작되었을 때 가장 높은 산소발생반응 활성을 보였다. 또한, $IrNiO_x$ 전극은 스프레이 방법으로 제작한 IrO_x 전극에 비해 높은 성능을 나타냈다. 이러한 결과는 Ir 에 Ni 를 도입함으로써 전기화학적 표면적이 증가했기 때문이다.

키워드: 양이온 교환 막 수전해, 음이온 교환 막 수전해, 기공구조, 수전해 내구성

학번: 2019-30419

List of Publication

1st or Co-1st Author

1. Chi-Yeong Ahn‡, **Sun Young Kang‡**, Hyuck Jae Choi, Ok-Hee Kim, Yung-Eun Sung, Yong-Hun Cho, "Effect of Anode Iridium Oxide Content on the Electrochemical Performance and Resistance to Cell Reversal Potential of Polymer Electrolyte Membrane Fuel Cells", *International Journal of Hydrogen Energy*, 2021, 46, 14713-14723.
2. Quang Luong‡, **Sun Young Kang‡**, Dohyeon Lee, Jihyeok Song, Mohanraju Karuppannan, Yong-Hun Cho, Oh Joong Kwon, "An effective strategy for preparing nickel nanoparticles encapsulated in polymer matrix-derived carbon shell with high catalytic activity and long-term durability toward urea electro-oxidation", *Materials Chemistry Frontiers*, 2021, 5, 4626.
3. **Sun Young Kang‡**, Ji Eun Park‡, Ga Young Jang, Ok-Hee Kim, Oh Joong Kwon, Yong-Hun Cho, Yung-Eun Sung, "High-performance and durable water electrolysis using a highly conductive and stable anion-exchange membrane", *International Journal of Hydrogen Energy*, 2022, 47, 9115-9126

Co-Author

1. Ok-Hee Kim‡, Chi-Yeong Ahn‡, **Sun Young Kang**, Sungjun Kim, Hee Ji Choi, Yong-Hun Cho*, Yung-Eun Sung*, "From Half-Cells to Membrane-Electrode Assemblies: a Comparison of Oxygen Reduction

Reaction Catalyst Performance Characteristics", *Fuel cells*, 2019, 6, 695-707.

2. Chi-Yeong Ahn‡, Juhee Ahn‡, **Sun Young Kang**, Ok-Hee Kim, Dong Woog Lee, Ji Hyun Lee, Jae Goo Shim, Chang Hyun Lee, Yong-Hun Cho*, Yung-Eun Sung*, "Enhancement of service life of polymer electrolyte fuel cells through application of nanodispersed ionomer", *Science Advances*, 2020, 6, 1-9.

3. Min Suc Cha‡, Ji Eun Park‡, Sungjun Kim‡, Seung-Hui Han, Sang-Hun Shin, Seok Whan Yang, Tae-Ho Kim, Duk Man Yu, Soonyong So, Young Taik Hong, Sang Jun Yoon, Seong-Heun Oh, **Sun Young Kang**, Ok-Hee Kim, Hyun S. Park, Byungchan Bae, Yung-Eun Sung*, Yong-Hun Cho*, Jang Yong Lee*, "Poly(carbazole)-based anion-conducting materials for fuel cells and water electrolyzers", *Energy & Environmental Science*, 2020, 13, 3633.

4. Mi-Ju Kim, Sungjin Kim, Ji Eun Park, Chan-Cuk Hwang, Seunggyeong Lee, **Sun Young Kang**, Daesung Jung, Yong-Hun Cho, Jaekook Kim, Kug-Seung Lee, Yung-Eun Sung, "Controlling active sites of Fe-N-C electrocatalysts for oxygen electrolysis", *Nano Energy*, 2020, 78, 105395.

5. Youngkwang Kim‡, Mohanraju Karuppannan, Dohyeon Lee, Hyo Eun Bae, Quang Thien Luong, **Sun Young Kang**, Yung-Eun Sung, Yong-Hun Cho*, Oh Joong Kwon*, "(Fe, Ni, Co)9S8@CS catalyst decorated on N-doped carbon as an efficient electrocatalyst for oxygen evolution reaction", *International Journal of Energy Research*, 2021, 1-10.

6. Chi-Yeong Ahn‡, Ji Eun Park‡, Sungjun Kim‡, **Sun Young Kang**, Wonchan Hwang, Min Her, Sungbin Park, Yong-Hun Cho*, Yung-Eun Sung*, “Differences in electrochemical performance of Pt-based catalysts for polymer electrolyte membrane fuel cells in liquid half-cells and single-cells”, *Chemical Reviews*, 2021, 121, 15075-15140

7. Chi-Yeong Ahn‡, Sungjun Kim‡, Hyuck Jae Choi, Jongmin Lee, **Sun Young Kang**, Ok-Hee Kim, Hyungwon Shim, Young-Shik Kim, Yung-Eun Sung, Oh Joong Kwon, Yong-Hun Cho, “Effect of iridium oxide as an additive on catalysts with different Pt contents in cell reversal conditions of polymer electrolyte membrane fuel cells”, *International Journal of Hydrogen Energy*, 2022, 47, 1863-1873.

8. Ji Eun Park‡, SungBin Park‡, Mi-Ju Kim, Heejong Shin, **Sun Young Kang**, Yong-Hun Cho, Yung-Eun Sung, “Three-Dimensional Unified Electrode Design Using a NiFeOOH Catalyst for Superior Performance and Durable Anion-Exchange Membrane Water Electrolyzers”, *ACS Catalysis*, 2022, 12, 135-145

9. Ok-Hee Kim‡, Hee Ji Choi‡, **Sun Young Kang**, Ga Young Jang, Mohanraju Karuppannan, Ji Eun Park, Yung-Eun Sung, Oh Joong Kwon, Yong-Hun Cho, “Towards Outstanding Performance of Direct Urea Fuel Cells Through Optimization of Anode Catalyst Layer and Operating Conditions”, *Journal of Electroanalytical Chemistry*, 2022, 921, 116661

10. Ji Eun Park‡, Hee Ji Choi‡, **Sun Young Kang**, Ga Young Jang, Ok-Hee Kim, Mohanraju Karuppannan, Yung-Eun Sung, Oh Joong Kwon, Yong-Hun Cho, “Effect of pore structures in nickel-based porous transport layers for high-performance and durable anion-exchange

membrane water electrolysis", *Journal of Energy Research*, 2022, 46, 16670-16678

11. Jihyeok Song‡, Youngkwang Kim‡, Hyo Eun Bae, **Sun Young Kang**, Jongmin Lee, Mohanraju Karuppannan, Yung-Eun Sung, Yong-Hun Cho, Oh Joong Kwon, "Effect of Precursor Status on the Transition from Complex to Carbon Shell in a Platinum Core-Carbon Shell Catalyst", *ACS Omega*, 2022, 7, 15615-15624